

https://dspace.org/

A veinhosted carbonate record of late Miocene to Pleistocene hydrothermal activity in the Hajar Mountains Jabal Akhdar Dome Sultanate of Oman

A Scharf; Robert Bolhar; T.I Uysal; F Mattern; et al

https://hdl.handle.net/10539/46266
WOS

Downloaded from a DSpace repository. https://dspace.org/

LITHOS 508-509 (2025) 108104

Contents lists available at ScienceDirect

LITHOS

journal homepage: www.elsevier.com/locate/lithos

A vein-hosted carbonate record of late Miocene to Pleistocene hydrothermal activity in the Hajar Mountains (Jabal Akhdar Dome, Sultanate of Oman)

A. Scharf [a,b,*], R. Bolhar [c], T.I. Uysal [d,e], F. Mattern [a], I. Callegari [f], G. Bozkaya [g], K. Baublys [e]

[a] Department of Earth Sciences, College of Science, Sultan Qaboos University, Sultanate of Oman
[b] UNESCO Chair on Ophiolite Studies, Sultan Qaboos University, Sultanate of Oman
[c] School of Geosciences, University of the Witwatersrand, South Africa
[d] Department of Geology, Istanbul University-Cerrahpasa, Turkey
[e] The University of Queensland, School of Earth and Environmental Sciences, Australia
[f] Department of Applied Geosciences, German University of Technology in Oman, Sultanate of Oman
[g] Department of Geological Engineering, Pamukkale University, Turkey

ARTICLE INFO

Keywords:
U–Pb carbonate dating
C-O stable isotopes
Fluid inclusions
Ediacaran
Fluid flow

ABSTRACT

The Jabal Akhdar Dome offers insights into the Neoproterozoic to Cretaceous geology of the Central Hajar Mountains in Oman. Ediacaran carbonates display Cadomian NW/SE-trending, non-plunging tight folds and SW-facing thrusts that are partly mylonitized. Calcite veins from the extended part of fold hinges of individual limestone layers and within faults/calc-mylonites provide six U–Pb ages ranging between 9 and 2 Ma. These ages are in conflict with field observations, indicating that pre-existing Cadomian(?) calcite veins were overprinted. Geochemically, vein carbonates display strongly positive Eu values in shale normalization ($[Eu/(0.5*Sm + 0.5*Gd]_{MUQ}$ = 1–8), indicative of precipitation from non-oxidizing hydrothermal fluids at temperatures >200–250 °C. The $\delta^{13}C$ and $\delta^{18}O$ values of the limestone host rocks range from +3.93 to +5.93 ‰ (V-PDB) and + 19.8 to +23.3 ‰ (V-SMOW), respectively. Vein calcites show slightly lower $\delta^{18}O$ values between 16.5 and 20.7 ‰ and considerably higher $\delta^{13}C$ values between +5.85 to +7.01 ‰. Homogenization temperatures from primary fluid inclusions in the calcite suggest precipitation at 125–160 °C (average of 142 °C). Stable isotope data are a product of a single calcite precipitation/recrystallization event, which required precipitation from fluids with similar temperatures and oxygen isotope compositions during fluid migration. Combined field geological, geochemical, isotopic, thermometric and petrographic observations suggest that original calcite within the Cadomian thrusts and fold hinges recrystallized at <10 Ma during a previously unknown hydrothermal event near the surface at temperatures of ~142 °C. This proposed hydrothermal event in the Jabal Akhdar at <10 Ma coincides with Late Cenozoic convergence of Arabia with Eurasia and/or India.

1. Introduction

The Jabal Akhdar Dome (JAD) of the Central Hajar Mountains (or Oman Mountains) offers a unique window into the style of deformation having affected Cryogenian to Ediacaran rocks (e.g., Scharf et al., 2021b). The Ediacaran Hajir (or Khufai) Formation, consisting of dark, organic-rich limestone, was overprinted by several deformation events. The oldest shortening events relate to the Infra-Cambrian Cadomian and Early Cambrian Angudan orogenies (Callegari et al., 2020; Scharf et al., 2021a). Subsequently, the region was affected by Permo-Triassic Pangea rifting (Blendinger et al., 1990; Chauvet et al., 2009; Le Métour et al., 1995; Mattern et al., 2024) and continental subduction during Late Cretaceous obduction of the Samail Ophiolite (e.g., Breton et al., 2004). Doming of the JAD occurred during the late Eocene to early Miocene (e.g., Corradetti et al., 2020; Grobe et al., 2018; Hansman et al., 2017). Finally, the region was affected by Oligocene/early Miocene and late Miocene to present-day deformation related to Arabia/India-convergence (Scharf et al., 2022b) and Arabia/Eurasia-shortening (Fournier et al., 2006). Exceptionally well-exposed, white calcite veins within a NE/SW-oriented, 100-m-long outcrop of the Hajir Formation

* Corresponding author at: Department of Earth Sciences, College of Science, Sultan Qaboos University, Sultanate of Oman.
E-mail address: scharfa@squ.edu.om (A. Scharf).

https://doi.org/10.1016/j.lithos.2025.108104
Received 4 January 2025; Received in revised form 17 April 2025; Accepted 19 April 2025
Available online 22 April 2025
0024-4937/© 2025 Elsevier B.V. All rights are reserved, including those for text and data mining, AI training, and similar technologies.

are thought to have formed during either the Cadomian Orogeny (NE/SW-shortening direction; Callegari et al., 2020) or continental subduction/exhumation during the Late Cretaceous (NE/SW-convergence; Zuccari et al., 2023).

Callegari et al. (2020) attributed extensional calcite veins in the outer parts of limestone beds in fold hinges to contractional Cadomian deformation. In the present study, U–Pb dating of these veins reveals consistent ages <10 Ma (late Miocene to Pleistocene), disagreeing with expected ages (Infra-Cambrian or Late Cretaceous). An understanding of the unexpected U–Pb ages necessitated further petrographic, trace element, isotope and fluid inclusion analyses. This holistic approach allowed a comprehensive assessment of the formation conditions of the dated calcite, with important implications for U–Pb dating of deformation-related carbonate formation.

In general, carbonate dating of various origins using the U–Pb technique since the early 1990s has provided significant improvements in the understanding of geological processes with multiple applications (i.e., speleotherms, tectonic evolution of carbonate platforms, fault dating, diagenesis; Rasbury and Cole, 2009; Roberts et al., 2020). Carbonate mineralized fractures and faults can be used to date the age of fluid flow, and when combined with structural analysis of the faults, they contribute to establishing or refining tectonic models (e.g., Carminati et al., 2020; Hansman et al., 2018; Ring et al., 2022; Ring and Bolhar, 2020; Smeraglia et al., 2020). Hydrothermal overprinting of fault-related vein carbonates in the field and U–Pb calcite ages may, therefore, provide information on later hydrothermal overprinting, following the initial vein precipitation event, or on a mixed age (Roberts et al., 2020; Roberts and Holdsworth, 2022). Hence, caution must be exercised when interpreting U–Pb calcite ages as they may not necessarily correspond to the timing of vein formation but rather register subsequent overprinting during separate tectonic events.

Our multi-disciplinary study investigates calcite veins from the Central Hajar Mountains, where the field relationships strongly suggest an Infra-Cambrian age of the calcite vein formation. To fully understand the conditions and timing of tectonic event(s) affecting the formation of the specific white calcite veins, we performed petrographic, geochemical, C–O stable isotope and fluid inclusion analyses in addition to U–Pb age dating of the calcite veins. This work aims (1) to better understand the tectonic evolution of Arabia, including the Hajar Mountains, and (2) to constrain the timing of a relatively young and previously unrecognized hydrothermal event during (re)precipitation/recrystallization of calcite veins.

2. Geological setting

The Hajar Mountains initially formed due to the Late Cretaceous obduction of the Neo-Tethys-derived oceanic lithosphere (Samail Ophiolite) and underlying deep-sea sediments (Hawasina) atop the Arabian Platform (e.g., Glennie et al., 1974). Eventually, the JAD was emplaced in the center of the Hajar Mountains (Fig. 1). Its doming

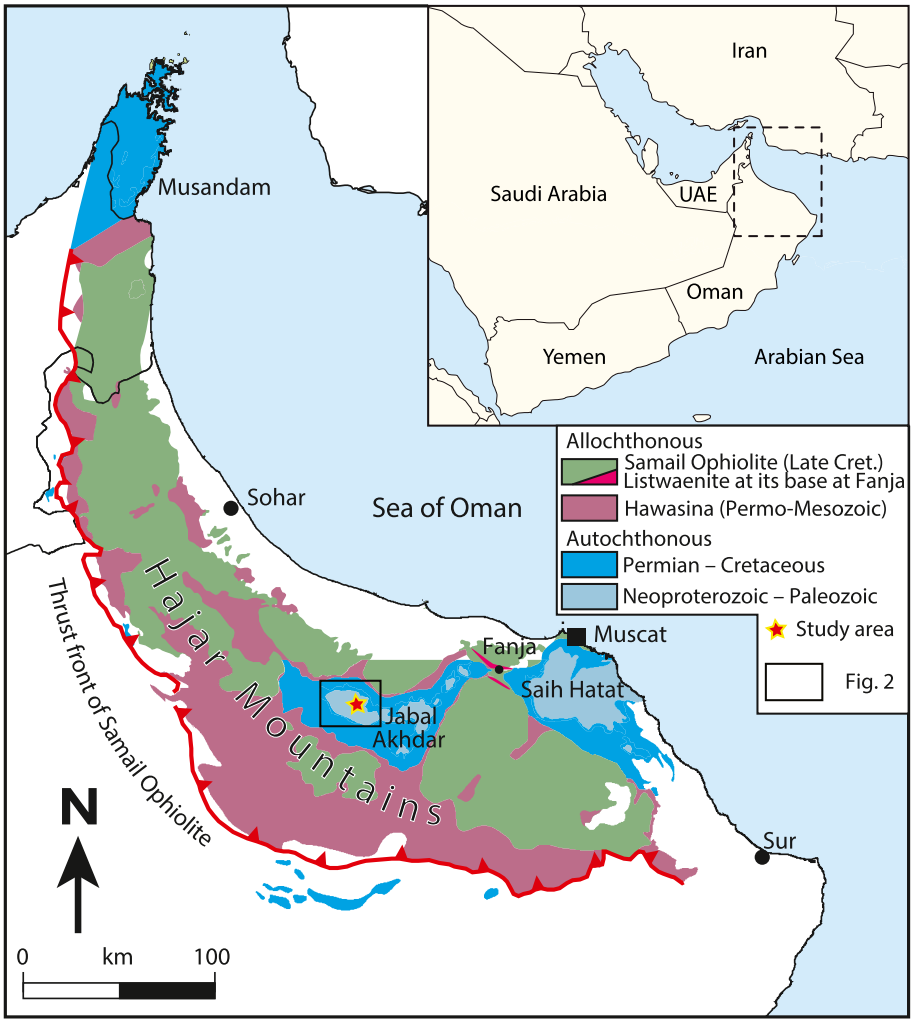


Fig. 1. Geological overview map of the Hajar Mountains and the study area located at the center of the JAD, modified after Forbes et al. (2010) and Callegari et al. (2022).

mainly occurred during the late Eocene and Oligocene (e.g., Corradetti et al., 2020; Hansman et al., 2017) and provides insights into the Arabian rocks that are well-exposed in the core of the dome (Fig. 2).

Within the JAD, the rocks consist of a succession of mostly siliciclastics and carbonates, deposited during the Neoproterozoic above a non-exposed Tonian crystalline basement (e.g., Glennie et al., 1974; Allen, 2007; Mattern and Scharf, 2019). According to Beurrier et al. (1986) and Rabu et al. (1986), the Neoproterozoic to possible earliest Cambrian rocks are the siliciclastic Mistal (>1500 m thick), carbonate Hajir (<100 m thick), siliciclastic Muaydin (800–900 m thick), carbonate Kharus (245 m thick) and siliciclastic/carbonate/volcaniclastic Fara (380 m thick) formations. These rocks are unconformably overlain by ~2.5 km-thick Permo-Mesozoic shelfal deposits (e.g., Rabu et al., 1986).

The Neoproterozoic rocks of the western-central JAD, close to our study area, witnessed two pre-Permian shortening events (Callegari et al., 2020; Scharf et al., 2021a). The older event, related to the Cadomian Orogeny, is characterized by a NE/SW-shortening direction with an inferred age between ~540 to 525 ± 5 Ma (Callegari et al., 2020). The younger event occurred at ~525 ± 5 Ma (Droste, 2014), is related to the Angudan Orogeny and associated with NW/SE-shortening (Callegari et al., 2020; Scharf et al., 2021a). Cadomian F1 folds are overturned and tight, with axes trending sub-horizontally to the SE or NW and amplitudes ranging between one and several tens of meters (Callegari et al., 2020). F1 axial planes dip gently towards the SW. Cadomian folds are best exposed in the Hajir Formation. F1 folds and thrusts, which sometimes truncate the folds, formed under ductile to brittle conditions at >150–250 °C, corresponding to depths of 6–8 km (Callegari et al., 2020). The younger Angudan F2 folds have an amplitude of 1–3 km, are tight and have sub-vertical axial planes striking NNE. F2 fold axes plunge moderately to the NNE or SSW (Callegari et al., 2020; Mann and Hanna, 1990; Rabu et al., 1986; Scharf et al., 2021a).

Following the Angudan event, the Jabal Akhdar area experienced tilting and block faulting before the formation of the basal-Permian (or 'Hercynian') unconformity (e.g., Rabu et al., 1986). Additionally, the wider region was impacted by Permo-Triassic Pangea rifting, resulting in SE-oriented extensional faults (e.g., Blendinger et al., 1990). After relative stable tectonic conditions during most of the Mesozoic, northeastern Oman was dragged into a NE-dipping subduction zone while the Late Cretaceous Samail Ophiolite was obducted (e.g., Breton et al., 2004; Ring et al., 2024). During subduction, rocks of the central JAD experienced temperatures of <250 °C and pressures of 0.2–0.4 GPa (Aldega et al., 2017; Breton et al., 2004). Zuccari et al. (2023) produced Late Cretaceous U–Pb aragonite ages from the same outcrop as our study area. Contrary to pressure-temperature estimates by Breton et al. (2004), they determined a peak temperature of ~350 °C using Raman spectroscopy on carbonaceous material and an inferred peak pressure of ≥0.9 GPa (based on the calcite-aragonite stability field) for carbonates of the Hajir Formation. Thus, rocks of the JAD may have been subducted to considerable depths, deeper than previously thought, during the obduction of the Samail Ophiolite.

Considerable doming and uplift (4–6 km) of the JAD took place during the late Eocene to Oligocene and some gentle uplift during the Miocene (Hansman et al., 2017). Uplift resulted in one expansive, open, NW/SE-trending, F3 fold of the Jabal Akhdar Dome. The fold axis of this late anticline is located 5 km south of the studied outcrop (Fig. 2). Low-temperature geochronology studies document that the JAD cooled to

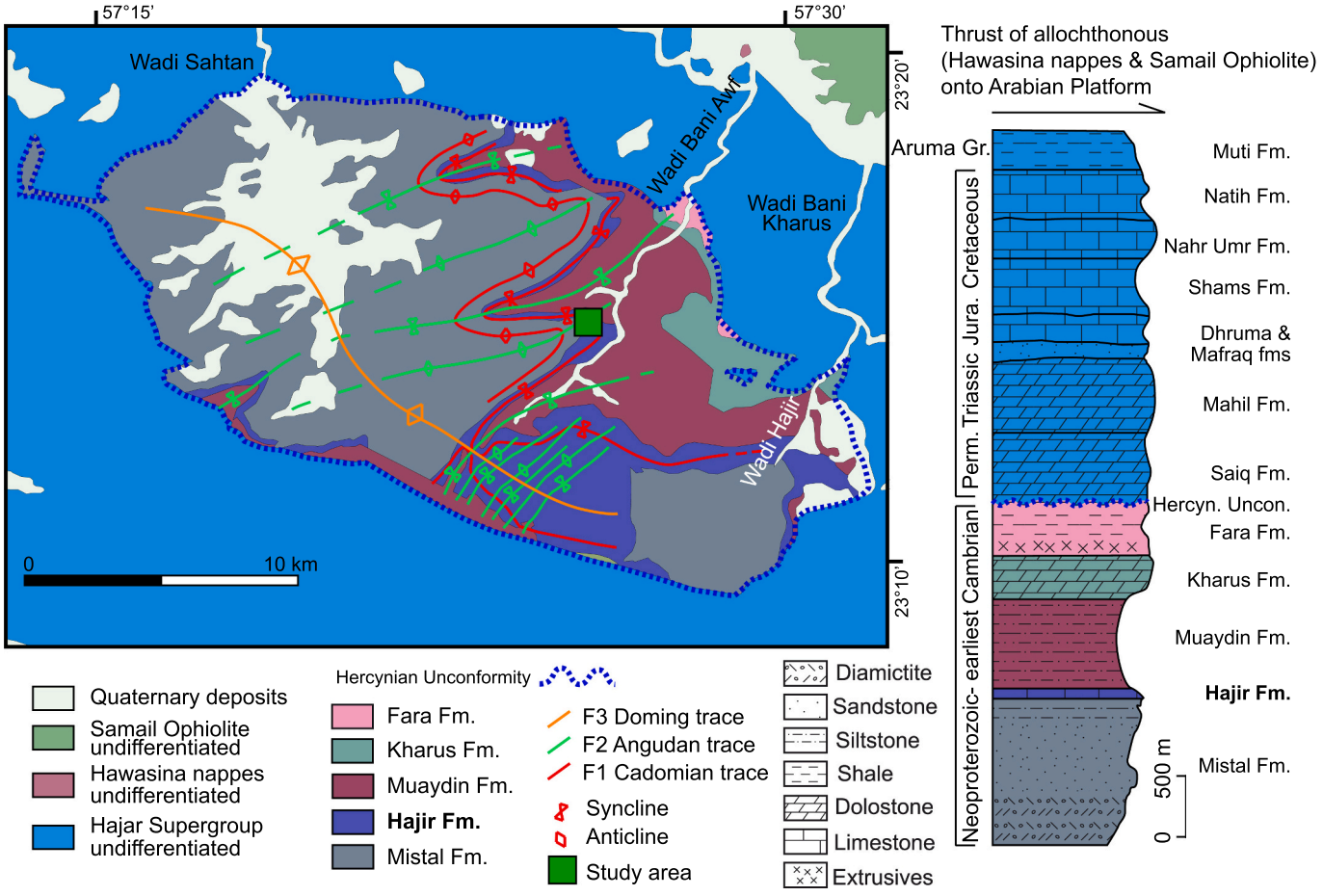


Fig. 2. Geological map and lithostratigraphic column of the western-central JAD, modified after Scharf et al. (2021a). The studied outcrop lies within the hinge zone of a large Angudan anticline of Wadi Bani Awf, in the core area of the JAD, and consists of limestone of the Hajir Formation.

temperatures of <50 °C at ~30 Ma (Corradetti et al., 2020; Hansman et al., 2017; Saddiqi et al., 2006). Late Eocene to Oligocene uplift may be related to the Arabia/Eurasia-convergence (Hansman et al., 2017) or to Eocene thermal erosion of the lithosphere below the Hajar Mountains related to the upwelling Afar Plume (Weidle et al., 2023) or a combination of both. Oligocene to early Miocene and late Miocene to present ~E/W-shortening due to the Arabia/India convergence affected eastern Oman, creating a sinistral, NW-striking wrench-fault corridor with a wrench-fault assemblage (Scharf et al., 2022a). Listwaenite bodies (fully carbonated/silicified peridotite) within the Samail Ophiolite are associated with E/W-striking extensional and NW-striking sinistral transtensional faults northeast of the JAD at Fanja (Fig. 1). Listwaenite has been dated using the U–Pb LA-ICP-MS technique as Early Cenozoic and Neogene to Pleistocene (Scharf et al., 2022b). Listwaenite requires substantial quantities of CO_2-rich fluids and forms metasomatically from peridotite along major extensional faults at near-surface conditions at temperatures <250 °C (Scharf et al., 2022b).

3. Methods

3.1. Field work

The structural inventory of the veins and associated folds, faults and ductile shear zones was documented in terms of dip direction/dip angle for planar fabrics and trend/plunge for linear features. Standard criteria for determining shear sense were applied in the field to assess fault kinematics. Structural data were plotted using Stereonet v. 11 by Rick Allmendinger (https://www.rickallmendinger.net/stereonet, date of last accesses 01/12/2022), using the algorithm provided by Allmendinger et al. (2012) and Cardozo and Allmendinger (2013), including determination of focal orientations of the fold axes and thrusts. Fold axes were determined by constructing the intersection linear of the fold limbs.

3.2. LA-ICPMS U–Pb geochronology

Uranium-Pb measurements were carried out in the Mass Spectrometry Facility at the University of the Witwatersrand, employing an Applied Spectra (formerly Australian Scientific Instruments) Resolution 193 nm ArF excimer (SE 155) system coupled to a Thermo Fisher Scientific sector-field ICPMS (Element XR). The measurements were performed in low resolution and electrostatic scanning (*E*-scan) modes. Data were acquired by single spot analysis (100 μm), using a laser repetition rate of 10 Hz and a fluence of 2.5 Jcm^{-2}. Total signal acquisition time was 50 s, allowing data processing and preparation for the next analysis, and twice comprising 10 s of pre- and post-ablation (gas blank) and 30 s of ablation measurements. Laser sampling took place in a dual-volume ablation cell (Laurin Technic, Canberra, Australia) using a mixed He–Ar atmosphere and a small volume of N_2 to enhance signal stability and sensitivity. The following gas flows were applied: He (300–400 ml/min), Ar (900–1050 ml/min) and N_2 (3–6 ml/min), respectively. Carbonate standard WC-1 (254 Ma; Roberts et al., 2017) served for primary calibration (Woodhead and Petrus, 2019), and Duff Brown limestone and Rio calcite were analyzed as unknown to evaluate accuracy and precision (Hill et al., 2016; Cris Lana, pers. communication). U–Pb isotope data are reported in Table 1. Additional details of the analytical setup (protocol, instruments, laser-spot maps) are provided in the Supplementary Material section (S1).

Duff Brown: This carbonate is a lacustrine limestone with ID-MC-ICPMS ages of 64.04 ± 0.67, 60.5 ± 4.6 and 66.3 ± 3.9 Ma (Hill et al., 2016). In our study 24 analyses combine to a lower intercept age of 73.76 ± 1.46 Ma (MSWD = 14). Anchoring to an initial $^{207}Pb/^{206}Pb$ composition (Kramers and Tolstikhin, 1997) of 0.82 produces an age of 75.02 ± 0.48 Ma (MSWD = 14). The lower age limit of the unanchored age is 8 % older than the 66 Ma age reported by Hill et al. (2016); however, our age overlaps within uncertainty with LA-ICPMS ages reported by Nuriel et al. (2017) and Drost et al. (2018) of 69.5 ± 3.5 Ma and 69.2 ± 3.7 Ma, respectively.

Rio calcite: This material is used as an in-house standard in the LA-ICPMS laboratory of Universidade Federal in Ouro Preto (Brasil) as well as at the University of the Witwatersrand, with an age of ~55 Ma (Cristiano Lana, 2020, personal communication). In our study, 19 analyses combine to a lower intercept age of 55.5 ± 0.8 Ma (MSWD = 8), which is identical to LA-ICPMS ages of 55 Ma previously reported in Ring and Bolhar (2020), Ring et al. (2022) and Scharf et al. (2022b).

Recommendations by Woodhead and Petrus (2019) were adopted to collect a minimum number of spot analyses (>30). Analyses resulted in MSWD values ranging from 3.6 to 9.6. Half of these are <4.5, which is slightly larger than the range (2–4) reported by Woodhead and Petrus (2019) for LA-ICPMS carbonate data. Analytical uncertainty on regressed ages are variable from 10 to 125 % SE (relative to regressed age), with the two most precise ages between 8 and 9 Ma and uncertainties of <1.5 Ma (2 SE absolute). Analytical uncertainty (2 SE) of individual spot analyses for $^{238}U/^{206}Pb$ ranges from 5 to 7 % for successfully dated samples (Table 1).

3.3. Geochemistry

Trace elemental analysis was carried out using the same instrumentation and analytical set-up as for U–Pb. Using low resolution and electrostatic scanning (*E*-scan) modes, data were acquired by single spot analysis (100 μm), using a laser repetition rate of 10 Hz and a fluence of 3 Jcm^{-2}. Laser settings and gas flow parameters are the same as described previously. Synthetic glass NIST 612 (Jochum et al., 2011) served for calibration while NIST610 and NIST614 glasses (Gao et al., 2002) were analyzed as unknowns. Tuning during line scans used NIST 612 glass for maximum sensitivity for ^{59}Co, ^{115}In and ^{232}Th at oxide levels (ThO^+/Th) <0.15 %. For internal standardization, the isotope ^{44}Ca was used. The following masses were measured: ^{24}Mg, ^{27}Al, ^{44}Ca, ^{51}V, ^{52}Cr, ^{55}Mn, ^{56}Fe, ^{59}Co, ^{60}Ni, ^{85}Rb, ^{88}Sr, ^{89}Y, ^{90}Zr, ^{137}Ba, ^{139}La, ^{140}Ce, ^{141}Pr, ^{146}Nd, ^{147}Sm, ^{151}Eu, ^{157}Gd, ^{159}Tb, ^{163}Dy, ^{165}Ho, ^{166}Er, ^{169}Tm, ^{174}Yb, ^{175}Lu, ^{206}Pb, ^{207}Pb, ^{238}U. All isotopes were measured in

Table 1
Summary of calcite samples, related structures and U–Pb age results.

Sample #Nr.	Description	Figure	Age	1 SE	2 SE	2 SE%	Av. Spot SE (%)	MSWD	n	outliers excluded
AS_20_10	Extensional vein in extended part of fold hinge of Fold 1	3a, b	4.89	3.05	6.1	125	7	3.6	47	22
AS_20_11	Extensional vein in extended part of fold hinge of Fold 1	3a, b	5.91	1.46	2.92	49	7	3.3	42	16
AS_20_13	Extensional vein in extended part of fold hinge of Fold 2	–	2.41	0.73	1.46	61	6	4.5	61	0
AS_20_14	Extensional vein in extended part of fold hinge of Fold 2	–	2.03	0.39	0.78	38	6	7.4	73	0
AS_20_16	Extensional vein above thrust	4a	8.95	0.46	0.92	10	6	9.6	97	0
AS_20_17	Thrust/calc-mylonite	3, 4a	7.71	0.72	1.44	19	5	9.1	89	5

triple mode, including pulse counting, analogue and Faraday cup, depending on signal. Data reduction was performed using the iolite extension, specifically the data reduction scheme ("DRS") "X_Trace_Elements_IS" (Paton et al., 2010, 2011).

3.4. C-O-Stable isotope analyses

The carbonate carbon and oxygen isotope compositions were determined in the Stable Isotope Geochemistry Laboratory at the University of Queensland using an Elementar Isoprime 100 dual inlet isotope ratio mass spectrometer (DI-IRMS) coupled to a multiprep block set to 90 °C. A total of 10 vein carbonates and 4 carbonate host rocks were subjected to analysis. Results were calibrated using international carbonate standards NBS18, NBS19 and USGS44 via a 3-point normalization for $\delta^{13}C$ and 2-point normalization for $\delta^{18}O$. The data are reported in per mil (‰) relative to V-SMOW for oxygen and V-PDB for carbon. Precision was calculated from laboratory calcite standard BCS, which was interspersed throughout each analytical cycle, with an analytical uncertainty for $\delta^{13}C$ of ±0.05 ‰ (1σ) and $\delta^{18}O$ ± 0.1 ‰ (1σ).

International standard values used for calibration.

Standard	$\delta^{13}C_{V\text{-}PDB}$‰	$\delta^{18}O_{V\text{-}SMOW}$‰
NBS18	−5.014	−23.2
NBS19	1.95	−2.2
USGS44	−42.21	

3.5. Fluid inclusions

Microthermometric studies of the fluid inclusions were carried out using a Linkam THMS 600 heating–cooling stage at Pamukkale University. The temperature of phase changes for eutectic melting (T_e), ice melting (T_{mice}) and homogenization to liquid or vapor (T_{hL} or T_{hV}) were recorded. Phase transitions below 0 °C are accurate to within ±0.2 °C based on calibration with pure CO_2 and H_2O standards at similar levels of precision. Above 0 °C, accuracy was ±2 °C based on the melting point of pure solids and synthetic fluid inclusion standards with a precision of ±1 °C. The ice-melting temperatures were converted to salinities using the equation of Bodnar (1993) and assuming that fluid composition is represented by the H_2O-NaCl system.

4. Results

4.1. Field Observations

The outcrop is located within a steep and narrow gorge known as "Little Snake Canyon". The start and end points are at 23°14′48.3"N/57°25′53.1″E and 23°14′53.7"N/57°25′55.1″E, respectively. Limestone of the Hajir Formation is medium- to thick bedded and dark gray to black. The well-exposed and 100-m-long outcrop is oriented subperpendicularly to the tight and overturned Cadomian folds and thrusts (Fig. 3a). The studied veins are associated with SW-dipping thrusts and are located in the extended part of the hinge zone of folded limestone layers of tight, NW/SE to NNW/SSE-trending overturned folds with a sub-horizontal axis. Veins are mostly bed-perpendicular in fold hinges. The vein/bed intersections are sub-parallel to the fold axes and the axial plane. Some thrusts are characterized by up to a few tens-of-centimeter-thick calc-mylonites (Figs. 3a, b, 4). Riedel faults, along with the low dip angle of the thrusts (~30°) and the orientation of the fold axes, which are sub-parallel to the strike of the thrusts, indicate that faults and calc-mylonites represent thrusts (Fig. 4), some of which may have been reactivated as extensional faults (Callegari et al., 2020). In addition to the described veins and fault planes, several <1-cm-thick, white and randomly oriented calcite veins intersect the rock near fault planes (Fig. 3).



Fig. 3. a) Overview photograph of a representative outcrop with a tight, overturned fold in the foreground. Near the center of the photograph, the fold is truncated by a calc-mylonite that traces the location of the thrust. The orientation of the thrust is sub-parallel to the fold axial plane of the overturned fold. A further thrust in the background is marked by white calcite. b) Close-up of the overturned fold with the calc-mylonite at the top. Note the white calcite veins in the extended part of the fold hinge but also some thin veins with various orientations.

The intersection lineation of <1 cm thick extensional veins from the fold hinge with the bedding is provided in Table S1 and Fig. 4c. The extensional veins in the fold hinges are sub-parallel to the axial planes (Table S1). These measurements provide proxies for the fold axes orientation. All thrusts and fold axes measurements are summarized in Fig. 4c. Direction of greatest horizontal shortening was NE/SW. Slickenlines on thrusts are sub-perpendicular to the fold axes (Fig. 4c), and thrusts are sub-parallel to the fold axial planes (Fig. 3).

The focal orientation of 15 measurements along nine thrusts is 218/24 (dip direction/dip angle; Fig. 4c). Slickenlines on thrust planes indicate a SW vergence. Eighteen measured and calculated fold axes as well as intersection lineations between extensional veins and the bedding within fold hinges trend sub-horizontally to the SE and NW (focal fold axis = 327/04; trend/plunge).

4.2. Petrography

The analyzed calcite crystals occur mainly as blocky vein fill (Fig. 5a-e). No aragonite was observed while calcite twinning is a common phenomenon. The type of calcite twins provides information on the deformation temperature. Burkhard (1993) and Ferrill et al. (2004) classified four calcite twin types. Type I (thin twins) represents the

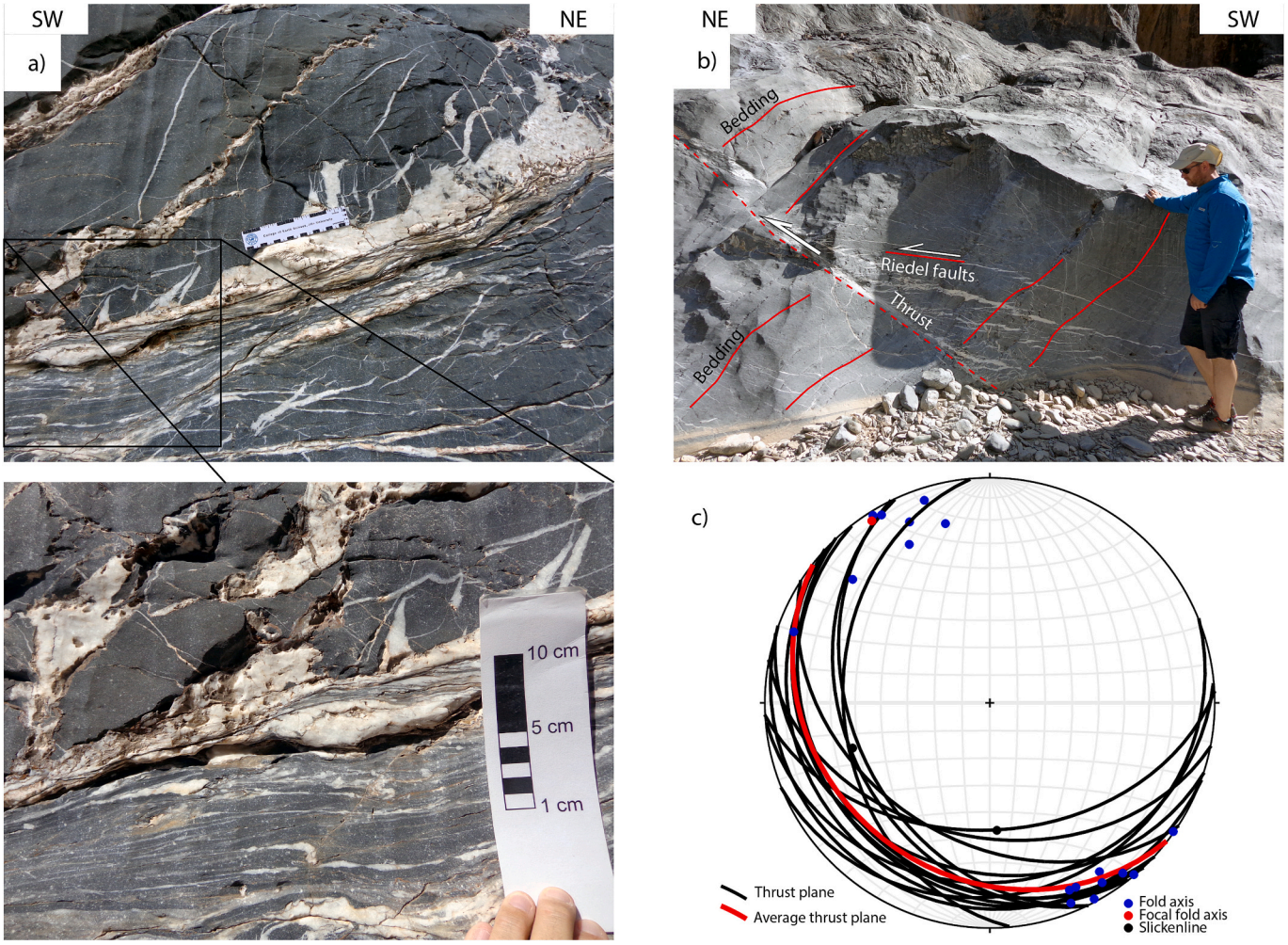


Fig. 4. a) Calc-mylonite of the thrust from Fig. 3 displaying ductile deformation of limestone. b) Thrust with Riedel faults indicating shear sense. c) Stereonet (lower hemisphere) compiling the structural measurements of the study area (utilizing Steronet v. 11 by Rick Allmendinger).

lowest temperatures while Type IV (thick patchy twins modified by dynamic recrystallisation) formed during highest temperatures. The large (>1 mm) and blocky calcite crystals often display twinning of Type I (thin twins) and Type II (tabular thick twins; Burkhard, 1993; Ferrill et al., 2004). In places, twins are slightly bent (Fig. 5c, d). Crystal boundaries are generally sharp (Fig. 5a) and locally display bulging recrystallisation (Fig. 5d).

Coarse calcite with large, subhedral to anhedral crystals often terminate at thin layers dominated by opaque material with sealing hiatuses preventing crystal growth (Fig. 5e). These opaque coatings or veneers are mainly composed of an iron oxide matrix mixed with small calcite particles representing a calcite gouge (Fig. 5e) (cf. Karabacak et al., 2022; Nuriel et al., 2012). The calcite gouges are interlayered with calcite veinlets (Fig. 5e) or contain calcite fracture network, resembling a breccia-like fabric (Fig. 5f).

A few thin calcite veins dissect the large blocky calcite crystals (Fig. 5c). One sample displays large calcite crystals with Type-I calcite twinning surrounded by a matrix of small calcite crystals also displaying Type-I calcite twinning (Fig. 5f). In some samples, blocky calcite crystals are brecciated and form clasts surrounded by the opaque matrix (Fig. 5e).

4.3. LA-ICPMS U–Pb carbonate ages

U–Pb ages are discussed below and graphically presented in Tera-Wasserburg diagrams (Fig. 6), where data points (2 SE) are color-coded according to $^{238}U/^{206}Pb$ ratios. Regressed lower intercept ages are reported at SE uncertainty using the software IsoplotR (Vermeesch, 2018). A summary of ages is provided in Table 1. Only six out of 14 samples provide U–Pb ages due to low U abundances, resulting in low count rates and associated high analytical uncertainties, also due to the limited spread of U/Pb ratios. Low U concentrations in fracture-filled carbonates, typically in the range of ~10 ppb to 10 ppm U, have been identified as a major limiting factor of LA-ICPMS carbonate dating (Roberts et al., 2020). Samples that failed to provide U–Pb ages are documented in the Supplementary Material (Table S2).

4.4. Trace element geochemistry

Minor and trace element geochemical data are reported in Table S3 and graphically displayed in Figs. 7 and S1. Rare Earth Element (REE) compositions for vein carbonates are normalized to Mud of Queensland (MUQ: Kamber et al., 2005). Concentrations of Mg and Mn range from 2679 to 5860 mg/kg and 118 to 299 mg/kg, respectively, while Fe contents are generally very low (below detection limits or < 40 mg/kg), confirming that all analyzed carbonates are pure $CaCO_3$. Very low concentrations of Al (from below detection limits of <6 mg/kg with the exception of two analyses with values of 125 and 330 mg/kg but also lowest total REE within each sample) document that the carbonates contain very little to no detrital material. Sr (2415 ± 341 mg/kg) concentrations are relatively uniform, and U (0.02 ± 0.03 mg/kg) and Pb (0.07 ± 0.07) define narrow and generally low abundances.

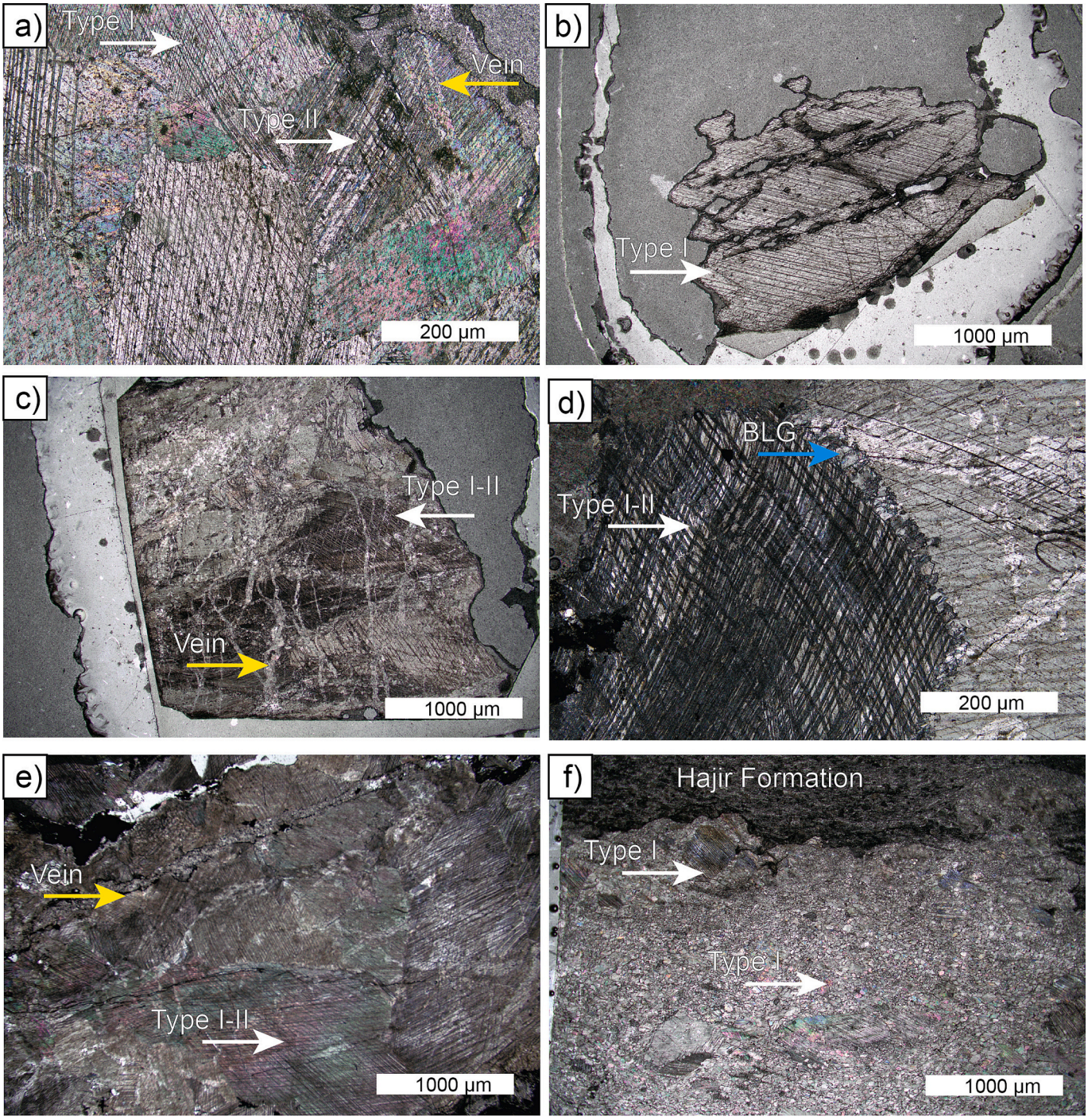


Fig. 5. Photomicrographs of vein gouge material as seen under cross-polarized light (XPL). (a) Sample AS-20-14 taken from a vein in extended part of a fold hinge displays large, blocky calcite crystals with Type I to Type II calcite twinning (arrows). Occasionally, small calcite-filled veins cut the large crystals (yellow arrow). (b) Sample AS-20-16, taken from extensional vein above a thrust, displays large calcite crystals with Type-I calcite twinning (arrow). (c) Sample AS-20-20 taken from a thrust. Large blocky calcite crystals with Type I to Type II calcite twinning (arrow) are cut by a network of thin calcite-filled veins (yellow arrow). (d) Sample JA-24-3 taken from a thrust. Detailed photograph of folded Type I to Type II calcite twins (arrow). Crystal boundary displays bulging recrystallization (BLG; blue arrow). (e) Sample JA-24-3 consists of large, blocky calcite crystals with Type I to Type II calcite twinning (arrow). Thin veinlet (yellow arrow) consists of an opaque iron oxide matrix. Locally, crystals are fractured with the fragmented calcite crystals being cemented by the opaque material. (f) Sample JA-24-4 is taken from a thrust. Top, dark part of the image displays the host rock (Hajir Formation). Within the vein, large calcite crystals with Type I twins (upper arrow) are surrounded by a matrix of small calcite crystals (lower arrow), which also display Type I calcite twins. (For interpretation of the references to color in this figure legend, the reader is referred to the web version of this article.)

Concentrations of U and Pb are similar to those reported for terrestrial vein carbonates (median U = 0.061, median Pb = 0.023 mg/kg: Roberts et al., 2020), although all types of carbonates (biogenic, diagenetic, speleothems and oceanic and terrestrial carbonates) largely overlap. Total REE range from 2 to 42 mg/kg, averaging 13 ± 10 mg/kg.

Normalized REE patterns are generally characterized by unfractionated Light REE (LREE), Medium REE (MREE) ($[La/Sm]_{MUQ}$ = 0.7–1.8), and depleted Heavy REE (HREE) ($[La/Lu]_{MUQ}$ = 0.9–12; $Sm/Lu]_{MUQ}$ =

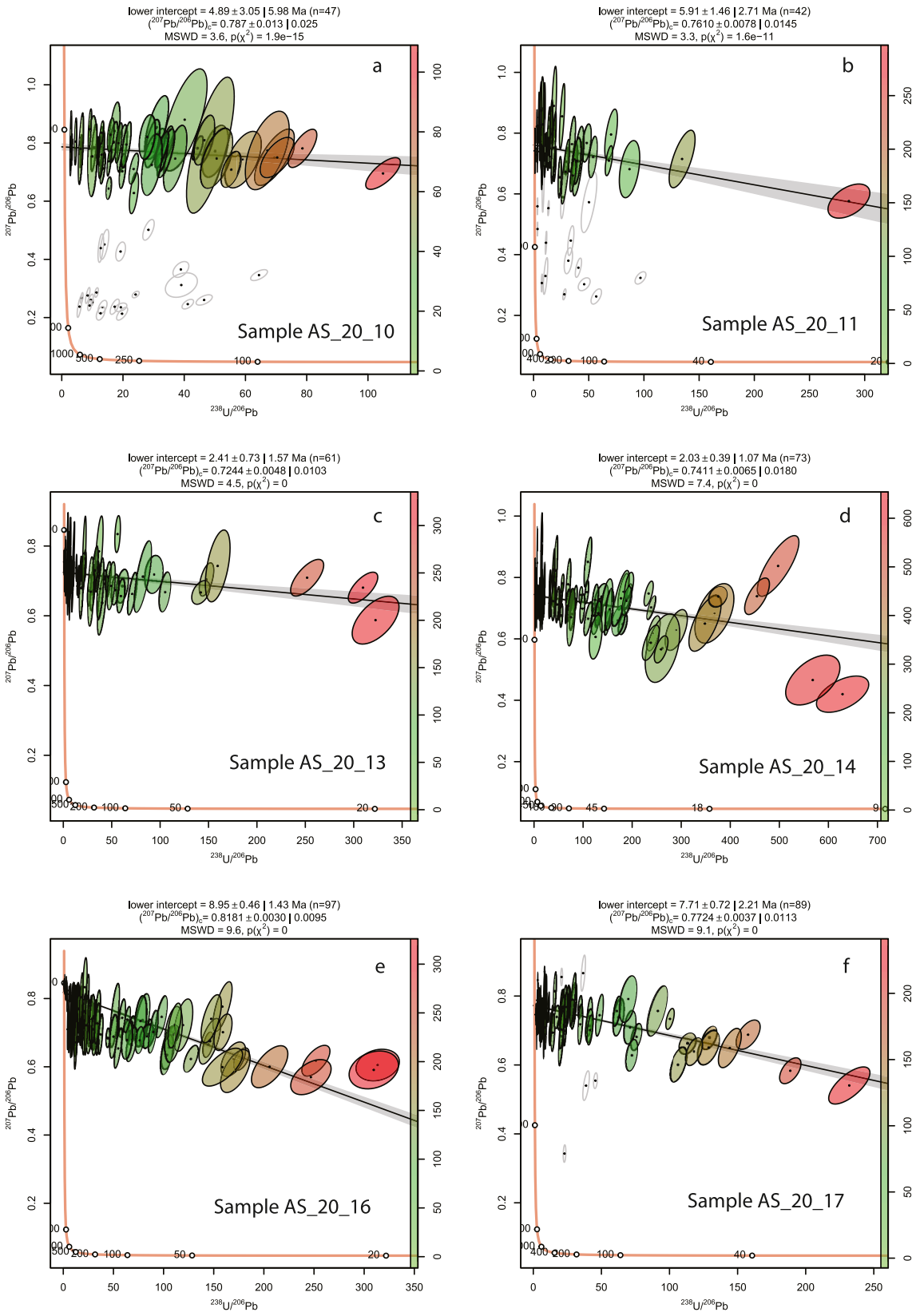


Fig. 6. Tera-Wasserburg diagrams showing U–Pb age data of six deformation-related carbonate samples; in all samples, calcite was dated; graphic representation and age calculation utilized IsoplotR (Vermeesch, 2018). Error ellipses represent two standard errors of mean; gray areas around discordia represent 2σ uncertainty of linear regression. Analytical precision (age, initial $^{207}Pb/^{206}Pb$) is indicated as analytical uncertainty (first value), "studentized 100(1−α)% confidence interval for t using the appropriate number of degrees of freedom" (second value) and "approximate 100(1−α)% confidence interval for t with over-dispersion, calculated as $z=y\sqrt{MSWD}$" (value 3). MSDW = mean squared weighted deviations; n = numbers of spot analyses. The U–Pb data ellipses are color-coded according to their $^{238}U/^{206}Pb$ value, displayed in the individual color scales at the right margin of the diagrams.

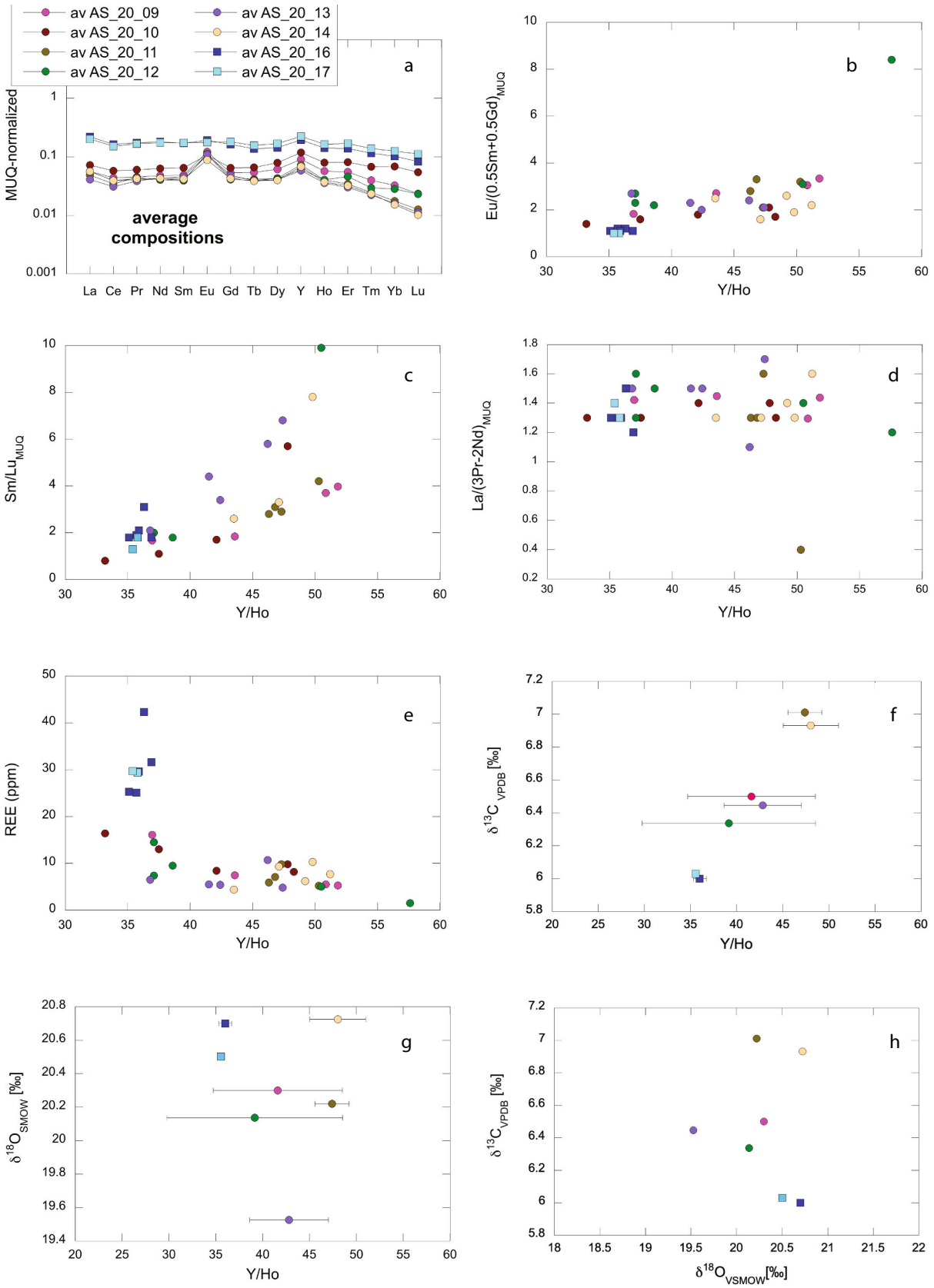


Fig. 7. a) Summary on REE patterns (overall average for each sample). Individual REE patterns are provided in Fig. S1. b-h) Diagrams showing trace element and isotopic compositions of carbonates; error bars in f and g are 1 SD of the mean. Averages were calculated using all analyses for each sample.

0.8–10) (Fig. S1). Almost all carbonates show strongly positive Eu ([Eu/(0.5*Sm + 0.5*Gd]$_{MUQ}$ = 1–8.4), subtle positive (La/3Pr-2Nd)$_{MUQ}$ = 0.4–1.7) anomalies and super-chondritic Y/Ho (33–58); Ce is not anomalous (Ce/2Pr-1Nd)$_{MUQ}$ ~ 1). Anomalies were calculated according to Bolhar et al. (2004).

4.5. Geochemical intra- and inter-sample variability

Comparison of trace element compositions for each sample allows examination of intra-grain variability. In most samples, the normalized REE compositions are similar to near identical, considering overall pattern, slope and elemental anomalies. Total normalized REE vary from 0.01 to 0.02, resulting in mostly parallel patterns and demonstrating uniformity of REE within samples (Fig. S1). In Sample AS_20_10, HREE are variable as a function of REE content; co-variability is also observed for Eu, with Eu anomalies increasing with decreasing REE. Lanthanum and Y anomalies are relatively uniform across all samples at logarithmic scale. Two analyses are anomalous: AS_20_11 shows an apparent Ce anomaly due to elevated Pr; since anomalous Pr cannot be explained by any geological process, it is likely an analytical artefact; Sample AS_20_12 yields measured concentrations of HREE below detection limits due to generally very low total REE. Inter-sample variability is assessed by comparing averaged REE patterns (Fig. 7a). With the exception of two samples, all carbonates show subparallel or identical patterns for LREE and MREE (Fig. 7a); this similarity does not extend to HREE with averaged compositions showing the lowest HREE with decreasing total REE. The similarity in compositions also applies to ubiquitous positive La, Eu and Y anomalies of similar extents. Averaged compositions for samples AS_20_16 and AS_20_17 show identical patterns, which are different to the majority of samples, with subtle positive anomalies for La and Y but lacking an Eu anomaly. When considering elemental ratios, carbonates display a continuum in Y/Ho (33–53), which is significantly correlated with Eu anomalies (Fig. 7b) and Sm/Lu (Fig. 7c) but uncorrelated with La anomalies (Fig. 7d). Several diagrams reveal strong correlations, either representing mixing relationships or operation of process(es) that systematically control REE and C isotope ratios: The strongest co-variabilities are observed for REE vs Y/Ho (Fig. 7e), d^{13}C vs Y/Ho (Fig. 7f) and Sm/Lu$_{MUQ}$ vs Y/Ho (Fig. 7c) while a weaker correlation is displayed for Eu/Eu* vs Y/Ho (Fig. 7b).

4.6. C–O Stable isotope analyses

The $\delta^{13}C$ and $\delta^{18}O$ values of the limestone host rocks range from +3.93 to +5.9 3 ‰ (V-PDB) and + 19.8 to +23.3 ‰ (V-SMOW), respectively. Vein calcites show slightly lower $\delta^{18}O$ values in a range between 16.5 and 20.7 ‰ (V-SMOW) and considerably higher $\delta^{13}C$ values, varying between +5.85 and + 7.01 ‰ (V-PDB) (Table 2).

Fluid $\delta^{18}O$ and CO_2 $\delta^{13}C$ compositions were calculated using calcite-water (O'Neil et al., 1969) and calcite-carbon dioxide (Chacko et al., 1991), respectively.

4.7. Fluid inclusions

Fluid inclusions were found to be scarce in the studied calcite, with sizes ranging from 5 to 15 μm. Fluid inclusion assemblages were identified based on the presence of liquid-vapor phases present at room temperature and criteria outlined by Roedder (1984). Primary inclusions are concentrated in zones, predominantly as two-phase (liquid + vapor), where fluid inclusions were concentrated in growth zones. These are liquid-rich and contain <50 vol% (mostly 10–30 vol%) vapor phase. Secondary inclusions are mostly liquid rich but rarely consist of two phases (liquid+vapor). Secondary fluid inclusions are located in trails (Fig. S2). A solid was determined in one inclusion which appears to be trapped (Sample AS_20_15).

Results of microthermometric analysis of fluid inclusions in three calcite vein samples (AS_20_15, AS_20_17, AS_20_20) within Ediacaran limestone are summarized in Table S4. Primary fluid inclusions are randomly oriented in the calcite while secondary fluid inclusion are rare and occur along trails, indicating micro-fractures (Fig. S2). Primary fluid inclusions in calcite formed during calcite formation while secondary fluid inclusions formed during a later fluid-migration phase. Eutectic melting was challenging to observe. One result of −58 to −55 °C is indicative of $CaCl_2$ in addition to NaCl in the fluid. The homogenization temperature of fluid inclusions varies between 125 and 160 °C (average 142 °C) in the primary inclusions and 200–260 °C (average 225 °C) in the secondary inclusions (Fig. 8). The only final ice-melting temperature of fluid inclusion data is −1 °C. By applying the equation of Bodnar (1993), fluid inclusion salinity is calculated from the melting temperature. The salinity value for that sample is 1.7 wt% NaCl equivalent. Calculated $\delta^{18}O$ values of CO_2 from fluids, from which three calcites precipitated at calculated temperatures, range from +1.9 to +9 ‰, +3.7 to +4.9 ‰ and from +7 to +14.1 ‰, +5.3 to +9 ‰, respectively (Table 2).

Table 2
Oxygen and carbon isotope data for carbonate samples.

Sample	$\delta^{18}O$ (‰ V-SMOW)	$\delta^{13}C$ (‰ V-PDB)	$\delta^{18}O$ (‰ V-SMOW)	$\delta^{13}C$ (‰ V-PDB)
	mineral	mineral	water at 142 °C	CO_2 at 142 °C
AS_20_9 vein	20.3	6.49	7.1	5.2
AS_20_10 vein	20.5	6.34	7.2	5.1
AS_20_11 vein	20.2	7.01	7.0	5.7
AS_20_12 vein	20.1	6.34	6.9	5.1
AS_20_13 vein	19.5	6.45	6.3	5.2
AS_20_14 vein	20.7	6.93	7.5	5.6
AS_20_16 vein	21.0	6.10	7.7	4.8
AS_20_vein	20.5	6.03	7.3	4.7
AS_20_18 vein	19.5	5.85	6.2	4.6
AS_20_20 vein	16.5	6.43	3.3	5.1
Hostrock 1	20.0	4.40		
Hostrock 2	23.3	3.93		
Hostrock 3	22.0	5.93		
Hostrock 4	19.8	5.29		

5. Discussion

5.1. Field geology

Thrusts, calc-mylonites and associated meter-scale overturned folds with extensional veins in limestone beds of the hinge area formed during the same tectonic event since the fold axial planes are oriented subparallelly to the thrusts (Fig. 3) and the fold axes are subperpendicularly oriented to slickenlines on the thrusts (Table S1). Furthermore, the extensional veins in the fold hinges are sub-parallelly oriented to the thrusts (Figs. 3, 4, Table S1). The orientation of the thrusts and overturned folds indicates shortening in NE-SW direction. This direction correlates with the Infra-Cambrian Cadomian event (Callegari et al., 2020) or Late Cretaceous obduction (e.g., Zuccari et al., 2023). Besides these structures, some randomly oriented thin calcite veins overprint all structures (Figs. 3, 4). We presume that these late, thin veins are related to hydrofracturing. A similar interpretation was provided for randomly oriented thin calcite veins in Mesozoic carbonates of the JAD (Bons et al., 2023).

5.2. Petrography

All investigated vein-calcite is similar in appearance using a petrographic microscope, regardless of compressional or extensional origin. This implies that both types formed under similar conditions. In general, calcite grains are large, blocky and display twinning (Type I to Type II; Burkhard, 1993; Ferrill et al., 2004; Fig. 5). These twins formed during deformation temperatures of <170 °C (Type I) to >200 °C (Type II; Ferrill et al., 2004). Dynamic recrystallisation of calcite is a dominant

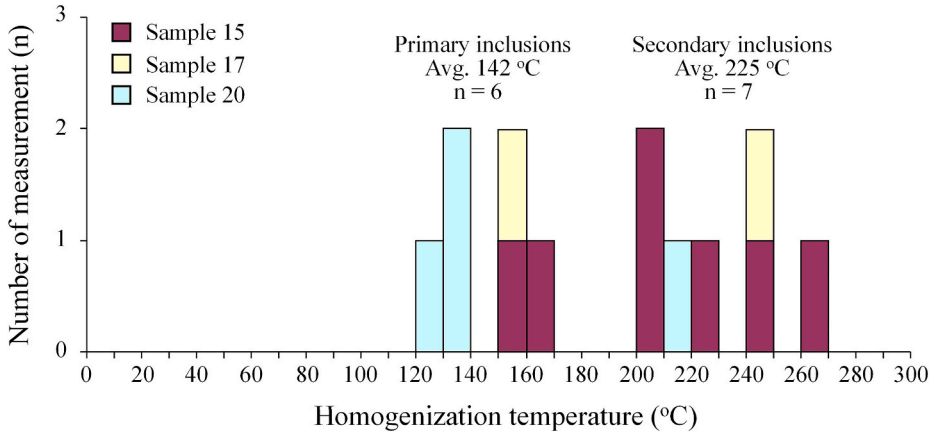


Fig. 8. Homogenization temperature (T_h) from primary (average 142 °C) and secondary (average 225 °C) fluid inclusions in calcite.

mechanism at temperatures >250 °C (Ferrill et al., 2004). Only at one location was bulging recrystallisation observed at the boundary of relatively large crystals (Fig. 5d). We conclude that the deformation temperature of the calcite crystals was <250 °C.

Locally, the calcite twins are slightly bent (Fig. 5d). This implies that some deformation affected the blocky calcite crystals after their formation. Calcite-filled micro-fractures with opaque minerals indicate hydrofracturing under brittle deformation conditions at temperatures <150–250 °C (Kennedt and White, 2001; Fig. 5e). Rock brecciation and gouge formation occurred in dilatational jog systems and in deformed country rocks during brittle faulting (Sibson, 1986).

5.3. U–Pb carbonate ages

The spread in $^{238}U/^{206}Pb$ is variable but generally high (>200: Sample AS_20_17 to >600: Sample AS_20_14) and, therefore, does not represent a limiting factor for obtaining precise ages in our study. Following the classification of Roberts et al. (2020), several scenarios can be recognized. In none of the dated samples are the datasets dominated by data points reflecting only common Pb (plotting to the left of the concordia; "type b"). However, most samples show a large proportion of common Pb-dominated carbonate with $^{238}U/^{206}Pb < 10$ (all five samples except for Sample AS_20_10). Samples AS_20_10 and AS_20_11 show mixed and scattered data, with a large number of points plotting well off and below the main regression line ("type c"). In these cases, addition or subtraction of parent U is unlikely as data points plot below concordia curves but at similar $^{238}U/^{206}Pb$ ratios when compared to the main array. A more likely cause of scatter is the addition of Pb with a composition significantly different to the regressed initial Pb. In all samples, the regressed initial $^{207}Pb/^{206}Pb$ ratios (0.72–0.82) are similar to the terrestrial common Pb isotopic composition at 10 to 3 Ma of ~0.82 (Kramers and Tolstikhin, 1997). In samples AS_20_14 and AS_20_16, data points may have shifted horizontally from the main array, indicative of U gain during open-system behavior ("type d"). None of the datasets resemble "type f", where carbonate contains strongly radiogenic Pb (with data points plotting close to the lower intersection with concordia), or "type g", where data points plot close to the upper intercept (with a reduced dispersion in U/Pb). The main limitation to obtaining highly precise ages or low MSWDs (<4) in our study is the large analytical uncertainty. These uncertainties are presumably due to low count rates because of low abundances of both U and Pb and the possibility of some degree of open system behavior (Sample AS_20_16). The relatively large data uncertainties prevent identification of possible inhomogeneity in ages (carbonates formed at different times or partially overprinted at a later time) or initial Pb. While this scenario is possible in samples AS_20_10 and AS_20_11, where outliers were excluded from regression, mixed ages are nevertheless unlikely considering the homogeneity of REE in each sample. None of the datasets conforms to "type h" and "i", where small uncertainties allow precise age determination, despite the large spread in $^{238}U/^{206}Pb$. While we acknowledge that uncertainties of regressed lower intercepts are relatively large, the six samples provide ages of 2.03 (±0.78), 2.41 (±1.46), 4.89 (±6.1), 5.91 (±2.92), 7.71 (±1.44) and 8.95 (±0.92) Ma (2 SE) that are significantly and consistently younger then U–Pb carbonate ages previously reported by Zuccari et al. (2023).

5.4. Controls on REE in carbonates

5.4.1. Influence of host rock mineralogy

Mineralogical control on REE can be considered minimal given that carbonates are mineralogically simple and uniform (Morgan and Wandless, 1980) and mostly consisting of calcium carbonate. Geochemical variability due to inadvertent analysis of detrital material is also unlikely given the low concentrations of trace elements diagnostic of detrital material (e.g., Al). The lack of strong compositional variability either rules out that distinct rock types were traversed as fluids percolated through the crust or that lithological heterogeneity did not affect fluid chemistry and, hence, the composition of carbonates. For instance, Permian hydrothermal carbonates from the Fichtelgebirge (Germany) documented variable REE compositions across various types of dolomites and calcites, including "roof-shaped" REE patterns; the latter were related to interaction of hydrothermal fluids with pelitic metasediments under acidic conditions (Hecht et al., 1999).

5.4.2. Hydrothermal effect on fluids

With the exception of samples AS_20_16 and AS_20_17, all analyzed carbonates display positive Eu anomalies, indicative of precipitation from hydrothermal fluids at temperatures >200 to 250 °C under non-oxidizing conditions (Bau et al., 2010). Suboxic conditions are confirmed by the general absence of negative Ce anomalies ($Ce/(2Pr–1Nd) \sim 1$), suggesting that fluids originated and interacted with host rock and precipitated carbonates at depths where redox conditions were not oxidizing. Ce oxidation is, in fact, considered to be limited to oxidizing sub-aerial environments (Bau and Möller, 1992). Positive Eu anomalies in hydrothermal fluids, such as those emanating from ocean floor vents, are due to the combination of high solubility of Eu^{2+}, comparable to Sr^{2+} (Shannon, 1976), and complexation with Cl (e.g., Craddock et al., 2010). Reduction of Eu is inhibited by elevated pH, and Eu^{2+} appears to be prevalent in aqueous solutions at temperatures of >200 to 250 °C (Sverjensky, 1984). However, because hydrothermally-induced Eu anomalies can be preserved in precipitates that form at considerably lower temperatures (Bau et al., 2010), a positive Eu is not always a reliable temperature indicator for precipitation of hydrothermal carbonates.

Most REE are trivalent and their behavior is governed by pH, sorption and complexation (Bau and Möller, 1992). Similar and overall low REE contents in all carbonates (Figs. 7a, S1) suggest that carbonate precipitation rates and/or solution flow rates were similar among all carbonates. Similar to Eu, Y (relative to its geochemical twin Ho) is enriched in hydrothermal fluids with ratios of ~75 and up to 200 (Bau and Dulski, 1995). Although such high values are not observed in vein carbonates in this study, most show slightly supra-chondritic (25–30 times; Fig. 7b-f) values of up to 57 times. Debruyne et al. (2016) noted that Y/Ho ratios are often elevated in hydrothermal carbonates and that total REE contents correlate with F (a proxy of F-complexation). Negatively correlated REE and Y/Ho suggest an absence of F-complexation (Fig. 7e).

5.4.3. Trace element signatures of marine vs hydrothermal origin

Principal fluid reservoirs for hydrothermal carbonate precipitation are sea-water, magmatic and meteoric waters. An addition and removal of REE occurs by mineral alteration, breakdown and precipitation during rock-water interaction (Debruyne et al., 2016). Contribution of sea-water or leaching of REE from marine (host rock) carbonate is indicated by a positive La anomaly in all carbonate samples, irrespective of total REE normalized REE patterns (Figs. 7e, S1). No geological process fractionates La from neighboring LREE other than what is observed for ancient and modern sea-water (Kamber and Webb, 2001). Therefore, REE were either sourced from sea-water or through leaching of REE from marine carbonate via fluid-rock interaction and isotopic exchange. Marine waters are characterized by elevated Y/Ho ratios and relative HREE enrichment (e.g., De Baar et al., 1985; Bau et al., 1997; Bolhar et al., 2004, Bolhar and Van Kranendonk, 2007, Bolhar et al., 2015) as well as negative Ce anomalies due to bacterially mediated oxidation and/or sorption to Fe–Mn oxides (Moffett, 1990; Bau and Dulski, 1995). Direct precipitation of vein carbonates from marine fluids is unlikely since La anomalies are unrelated to Ce anomalies and Y/Ho (Fig. S1). Lanthanum anomalies were most likely inherited from marine carbonates during equilibration with fluids that eventually precipitated the vein-hosted carbonates. Furthermore, HREE enrichment in shale-normalization and subtle positive Gd anomalies are not observed in the vein carbonate, being diagnostic for a marine origin of REE. A lack of correlation with Ce and Y is plausibly explained by hydrothermal fluid-rock interaction: elevated and non-chondritic Y/Ho can be caused by Fl, Cl? complexation (Bau and Dulski, 1995). Sorption by Fe–Mn oxy-hydroxides (Bau et al., 1996) or mineralogical control (Tanaka and Kawabe, 2006) is unlikely due to the lack of petrographic evidence for mineralogical variability or the presence of Fe-oxides (Fig. 5). A marine Ce signal was diminished due to hydrothermal activity under reducing conditions.

5.4.4. Other processes and factors controlling REE in fault-hosted carbonates

Post-depositional alteration with calcite-undersaturated fluids may have affected “primary REE” compositions and U–Pb systematics, resulting in isotopic resetting and apparent young post-depositional ages. Ce anomalies may indicate post-depositional remobilization in near-surface environments (Bau and Dulski, 1995). A lack thereof in the vein carbonate samples (Figs. 7a, S1) rules out oxidative overprinting, especially since this process would have reduced or obliterated positive Eu anomalies (Bau and Möller, 1992). The resilience of REE during post-depositional recrystallisation and diagenesis has been documented for marine carbonate that underwent multi-stage and regionally extensive dolomitization (Banner et al., 1988).

Hydrothermal fluids could have been sourced magmatically (Yardley and Bodnar, 2014; Veksler, 2004); exsolved magmatic fluids have generally elevated REE + Y concentrations (up to ppm) (Debruyne et al., 2016). While relatively little data are available to fully characterize magmatic fluids, they tend to be enriched in LREE and strongly depleted in Eu (e.g., Banks et al., 1994). A significant contribution of magmatic fluids appears unlikely, considering the uniformity of LREE and Eu with a general lack of LREE enrichment and Eu depletion in all vein carbonate samples.

Under hydrothermal conditions and with increasing temperature, complexation with hard ligands (Cl^-, F^-, OH^-, CO_3^{2-}, PO_4^{3-}, SO_4^{2-}) increasingly aids in solubility and transport of REE + Y (Haas et al., 1995). Under alkaline conditions (and down to pH ~ 3), hydroxide complexation dominates (Pourtier et al., 2010), although species are largely insoluble, thus, limiting transport. Carbonate and phosphate complexes are likewise prevalent but insoluble. Complexation by different species and variable solubility at hydrothermal conditions is documented in Fig. 7d, where total REE show a convex-upward co-variation with Y/Ho, the latter reflecting increasing hydrothermal imprint on trace element compositions. For instance, while REE-F species are considerably more stable than REE-Cl complexes at elevated temperatures, they are also largely insoluble over a wide range of pH, limiting their ability to keep REE in solution and hindering transport (Debruyne et al., 2016). Other important hydrothermal complexes are REE-Cl and, to a lesser extent, REE-SO_4-F (e.g., Migdisov and Williams-Jones, 2014). Heavy REE complexes are more stable at ambient and higher PT conditions (Van Sijl et al., 2009), especially as carbonate species (Lee and Byrne, 1992; Tsay et al., 2014). Chloride complexation under hydrothermal conditions is poorly constrained, although Cl and F seem to favor LREE (Debruyne et al., 2016). In this context, the lack of LREE enrichment in all vein carbonates points to a lack of Cl and F complexation, but an expected dominance of carbonate complexation. The correlated behavior of Eu, HREE with Y/Ho (Fig. 7b, c) possibly reflects temperature control. A lack of increasing HREE/LREE and Y/Ho ratios observed in the vein carbonates rules out surface complexation (sorption) (Bau and Möller, 1992; Debruyne et al., 2016). Sorption-dominated regimes favor LREE enrichment (not observed in most analyzed samples), while HREE enrichment is enhanced in complexation-dominated systems (Bau, 1991). The variability of HREE relative to MREE (mostly in Sample AS_20_10; Fig. S1) can, therefore, be explained by complexation.

Finally, Rayleigh fractionation and co-precipitation of REE-enriched minerals are explored. Monazite is especially enriched in the LREE and, considering its widespread occurrence in upper crustal rocks and its very low solubility in aquatic fluids, can influence REE + Y in hydrothermal systems (e.g., Debruyne et al., 2016; Wood, 2004). Co-precipitation of monazite and Rayleigh fractionation of other LREE-enriched minerals would significantly deplete LREE in hydrothermal fluids and result in LREE depleted normalized REE + Y patterns; based on REE patterns for vein carbonates (Bau and Möller, 1992), this possibility is ruled out.

In summary, major and trace element data document fairly homogeneous compositions within and between different vein carbonates. Most vein carbonate displays consistent positive anomalies for La, Eu and Y. Direct involvement of seawater (percolation into crustal levels) is not supported. Instead, REE were inherited through leaching from primary marine Ediacaran carbonate when fluids percolated through host rocks. Correlated Eu anomalies and suprachondritic Y/Ho provide evidence for hydrothermal activity and complexation by carbonate. The absent Ce anomalies document precipitation under anoxic conditions. Hydrothermal overprinting would have likely caused resetting of the U–Pb system.

5.5. C–O stable isotopes

Stable isotope data seem to be the product of one calcite precipitation or recrystallization event since $\delta^{18}O$ values of vein calcite represent a fairly narrow range between +19.5 and 21 ‰ (except one outlier of 16.5 ‰). Precipitation occurred from fluids with similar oxygen isotope composition at similar temperatures. Primary fluid inclusion homogenization temperatures of ~125 to ~160 °C (average of 142 °C, Fig. 8) correspond to estimated fluid $\delta^{18}O$ values of +3.3 and 7.7 ‰ (V-SMOW) (Table 2). This range of isotopic value is characteristic of deep formation

waters in sedimentary basins or metamorphic fluids (Evans et al., 2008; Hoefs, 2021). Alternatively, it may have resulted from pronounced interaction of local meteoric fluids with host rock at low water-rock ratios (isotopic buffering of the fluid by the host rock; Beaudoin et al., 2022).

Values of $\delta^{13}C$ of both the Ediacaran host rocks and the vein carbonate are distinctively elevated with positive values, and higher than $\delta^{13}C$ values of limestone that vary mostly within a range of 0 ± 3 ‰ since the Archean (Hoefs, 2021). However, a positive carbon isotope excursion with $\delta^{13}C$ values up to +8 ‰ is documented to have occurred

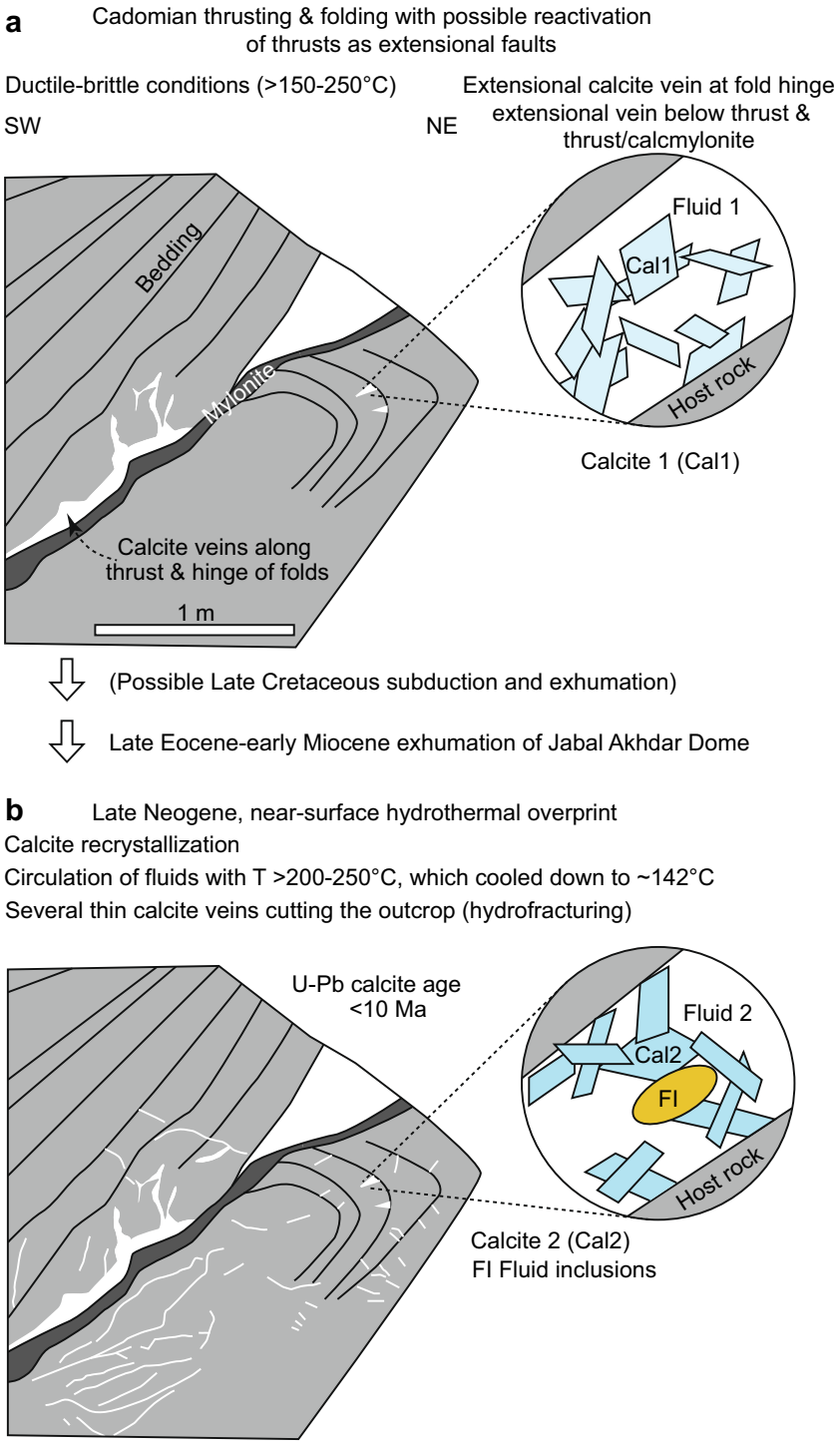


Fig. 9. Summary of calcite vein development in Wadi Bani Awf. a) Cadomian thrusting and associated folding produced calc-mylonites and extensional veins in the fold hinges. Precipitation of Calcite 1. Ductile deformation occurred at temperatures of >150–250 °C. b) After possible Late Cretaceous subduction and exhumation as well as late Eocene-early Miocene exhumation, the rocks were overprinted by a Late Cenozoic hydrothermal event. Initial metamorphic fluids were non-oxidizing and equilibrated at temperatures of >200–250 °C (based on Eu-anomalies). Fluids cooled down to ~142 °C (primary fluid inclusions in Calcite 2) and precipitated calcite at <10 Ma. Local and minor late-stage overprint during the same event produced secondary fluid inclusion at ~225 °C. Calcite microstructures (twins, minor dynamic recrystallization) confirm that Calcite 2 was deformed at temperatures between <170 and 250 °C. Carbon and oxygen isotope signatures of Calcite 2 are adopted from the host rock and deep metamorphic fluids, respectively. Calcite 2 preserves the geochemical trace element fingerprint of Cadomian(?) Calcite 1.

in Neoproterozoic (Late Riphean) marine carbonates (Derry et al., 1992). Thus, $\delta^{13}C$ values of the Ediacaran host rocks represent a positive carbon isotope excursion similar that reported for the Hajir Formation (Khufai Formation) from Wadi Hajir 10 km to the southeast of our study area (Ostrander et al., 2023; Fig. 2).

Compared to the host limestone, the vein samples have even higher $\delta^{13}C$ values (Table 2). Considering that carbon isotope fractionation at relatively low temperastures (100–150 °C) is insignificant (Chacko et al., 2001), the higher $\delta^{13}C$ values of the vein samples indicate disequilibrium between the fluids and the host rock at the time of calcite precipitation. Although $\delta^{13}C$ values of the vein carbonate are likely buffered by their host rock to some extent, an additional mechanism for the increase in ^{13}C in veins is required. Bacterial fermentation and methanogenesis in shallow marine environments are known to produce extremely large fractionation with bacterial light CH_4 and heavy CO_2 ($\delta^{13}C$ up to +15 ‰) (Mozley and Wersin, 1992). However, $\delta^{13}C$ values of the vein carbonate cannot result from inheritance of significantly ^{13}C-enriched early diagenetic carbonates in the limestone because the veins are associated with a much younger (U–Pb ages) tectono-thermal process that took place at much higher temperatures then early diagenesis. By analogy with thermogene travertines, where CO_2 derives from sub-surface thermal processes, non-equilibrium gas-transfer isotope fractionation occurs during intense CO_2 escape from water, with ^{12}C preferentially fractionated into the gas phase, and ^{13}C being enriched in the residual fluid (Evans et al., 2008; Uysal et al., 2009). Vein carbonate is, therefore, most likely a product of hydrothermal activity or precipitation from deeply circulating fluids that reached deep crustal levels at temperatures >250 °C (before the near surface vein formation). Non-equilibrium carbon isotope fractionation seems to be the most plausible explanation for the increase in ^{13}C in veins (e.g., Evans et al., 2008).

5.6. Tectonic model

Overall, the WNW/ESE-striking thrusts and veins were most-likely filled with Cadomian calcite 1 (Fig. 4a, b). The orientation of these structures and the fold axes is consistent with NE/SW-directed Infra-Cambrian (Callegari et al., 2020) or Late Cretaceous (Zuccari et al., 2023) deformation (Fig. 9). Folds, thrusts and veins formed during the same deformation event (Section 5.1). The fact that some faults are calc-mylonites demonstrates that the formation of these structures (Infra-Cambrian and possibly Cretaceous) must have occurred at temperatures >150–250 °C (Kennedt and White, 2001). Late Cretaceous calcite U–Pb ages provided by two veins from the same studied outcrop yield ages of 96.5 ± 31.6 and 97.5 ± 23.3 Ma (2 SE; Zuccari et al., 2023). We did not obtain any Cretaceous ages from our own U–Pb age measurements.

We suggest that the calcite-1 filled faults and folds (with the extensional veins in the fold hinges) formed primarily during the Cadomian Orogeny. Alternatively, the brittle thrusts and folds could have been active during the Late Cretaceous indicating deformation during continental subduction based on the U–Pb ages obtained by Zuccari et al. (2023), Fig. 9a. Eventually, rocks cooled to near-surface temperatures (<50 °C) during the exhumation of the JAD during the late Eocene to early Miocene (Hansman et al., 2017).

The study area must have been affected by renewed tectonics, associated with hydrothermal fluid migration and recrystallization of calcite 2 at <10 Ma, based on the U–Pb calcite ages and the REE geochemistry. Calcite 2 is blocky, large and relatively pure with a homogenous composition within the sample and between different veins (Section 5.4). The positive La, Eu and Y anomalies of Calcite 2 demonstrate that the fluids are not primarily derived from seawater. The Y/Ho and $\delta^{13}C$ values show that hydrothermal fluids were sourced from leaching of marine carbonate of the Hajar Formation. The geochemical fingerprint of the carbonate, i.e., Eu anomalies, suprachondritic Y/Ho and absence Ce anomalies, indicates that the fluid circulation associated with the hydrothermal event occurred at temperatures reaching >200–250 °C under non-oxidizing conditions (Fig. 9). This temperature was reached during fluid circulation at depth before Calcite 2 precipitation took place at lower temperatures of 125–160 °C (based on primary fluid inclusions). The idea of hydrothermal fluid migration is supported by the occurrence of variably oriented thin calcite veins in the entire outcrop (Figs. 3, 4), indicating hydrofracturing (Fig. 9b).

Fluid inclusion examination confirms that two fluid phases affected the calcites. The primary and secondary fluid phases had different temperature ranges. The secondary fluid inclusions (~225 °C) are minor and can be found along trails within Calcite 2 (Fig. S2). Because secondary fluid inclusions are minor, we assume that the amount of the respective fluids was insufficient to fully overprint the calcite. Thin section petrography confirms that the vein calcite crystals from thrusts and extensional veins display a similar appearance. The blocky, large crystals were deformed at temperatures between <170 °C and 250 °C (calcite twins and minor bulging recrystallization; Section 5.2). Locally folded calcite twins, brecciated calcite and thin calcite veins with opaque minerals demonstrate brittle deformation and fluid flow after calcite twinning. The calcite carbonate isotope signature is influenced by interaction with the Ediacaran host rock, while the oxygen isotope

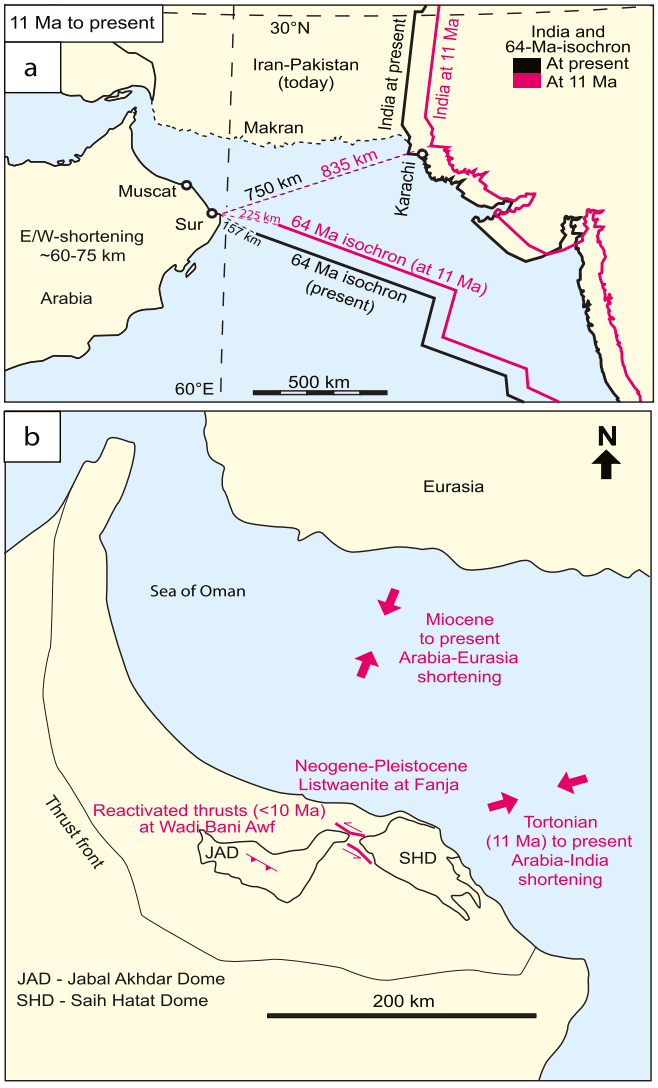


Fig. 10. Paleogeographic reconstruction of the greater study area from 11 Ma until present, modified from Scharf et al. (2022b). a) Arabia/India-shortening amounts to ~60–75 km from 11 Ma until present. b) ENE/WSW Arabia/India and/or NE/SW Arabia/Eurasia-shortening may account for reactivation of NW-striking thrusts in Wadi Bani Awf and NW-striking listwaenite bodies, associated with sinistral faults near Fanja, located between the JAD and SHD.

signature is related to deep metamorphic fluids.

On a regional scale, the strike of the NW/SE-veins and thrusts is similar to many listwaenite bodies in the Fanja area, located ~70 km to the NE of the study area (Scharf et al., 2022a; Fig. 1). Listwaenite, which requires substantial quantities of CO_2-rich aqueous fluids, has a Neogene to Pleistocene age (Scharf et al., 2022a) and is similar in age to the studied calcite veins in Wadi Bani Awf. The geochemistry of the calcite veins of Wadi Bani Awf strongly indicates a hydrothermal origin with some possible chemical assimilation of (older?) host rock calcite. The most plausible explanation for all geochemical and isotopic data is that the calcite veins in Wadi Bani Awf formed during the same tectonic event as the Neogene to Pleistocene listwaenite in Fanja, at near-surface conditions.

Possible tectonic event(s), responsible for the formation of the <10-Ma-old calcite in Wadi Bani Awf and Miocene/Pleistocene listwaenite in the Fanja area are either ongoing NE/SW-directed shortening between Arabia and Eurasia, starting before ~25–23 Ma (Agard et al., 2011), and/or ENE/WSW-directed shortening between Arabia and India (Fournier et al., 2006). The latter amounts to shortening of ~60–75 km, starting ~11 Ma ago and continuing until present-day, as demonstrated by GPlates reconstruction (Scharf et al., 2022b; Fig. 10). NW-striking faults in Wadi Bani Awf are favorably oriented to be reactivated during NE/SW to ENE/WSW-oriented shortening.

6. Conclusions

This study is the first to report age-constrained hydrothermal activity in the JAD. Uranium-Pb calcite of <10 Ma, combined with petrography, geochemical and C–O stable isotope data as well as fluid inclusion analyses, demonstrate that calcite-filling of possibly Cadomian fractures must have been formed/recrystallized during a hydrothermal event during the late Miocene to Pleistocene.

The Neogene to Pleistocene hydrothermal event of the central JAD is coeval with listwaenite formation adjacent to the dome at Fanja. This is supported by the similar NW-strike of the calcite veins and the listwaenite bodies. Tectonic events(s) associated with hydrothermal activity and fluid migration are the Arabia/Eurasia and/or Arabia/India convergence, producing NW-oriented faults (Scharf et al., 2022b). Taking into account the occurrence of metasomatic rocks near Fanja (listwaenite) as well as carbonates with a hydrothermal geochemical signature documented in the current study, we suggest that late Miocene to Pleistocene hydrothermal activity in eastern Oman was widespread.

Uranium-Pb dating of calcite veins related to faults must be evaluated with caution. Even though field relations seem to provide a clear picture of the relative calcite vein formation age and its tectonic origin, such interpretations can be misleading when the study area was hydrothermally overprinted. U–Pb calcite ages, in combination with petrography, geochemical, stable carbon and oxygen isotope data as well as fluid inclusions should be performed to reveal the full tectonic history of calcite veins, and where plausible, to consider a possible hydrothermal overprint.

CRediT authorship contribution statement

A. Scharf: Writing – original draft, Visualization, Project administration, Methodology, Investigation, Funding acquisition, Formal analysis, Conceptualization. **R. Bolhar:** Writing – review & editing, Visualization, Resources, Methodology, Investigation. **T.I. Uysal:** Writing – review & editing, Visualization, Methodology. **F. Mattern:** Writing – review & editing, Methodology, Investigation. **I. Callegari:** Writing – review & editing, Methodology, Investigation. **G. Bozkaya:** Writing – review & editing, Methodology. **K. Baublys:** Writing – review & editing, Methodology.

Declaration of competing interest

The authors declare that they have no known competing financial interests or personal relationships that could have appeared to influence the work reported in this paper.

Acknowledgments

We thank Hamdan Al-Zidi and Bader Al-Waili (both Sultan Qaboos University) for sample preparation. Katharina Scharf is thanked for field assistance. AS acknowledges funding by Sultan Qaboos University (IG/SCI/ERTH/21/01). The LA-SF-ICPMS facility at the University of Witwatersrand was funded by an NRF-NEP grant (UID 105674) to RB. An earlier version of the manuscript was reviewed by two anonymous reviewers and the Editor, Taylor Schildgen. The manuscript improved thanks to the one anonymous reviewer and Aley El-Shazly, as well as the Editor Ali Polat. We thank S. Mattern for English proofreading. Additional information as mentioned in the text is available in the Supporting Material section.

Appendix A. Supplementary data

Supplementary data to this article can be found online at https://doi.org/10.1016/j.lithos.2025.108104.

Data availability

Data archived in a repository: All file data are presented in the Supporting Information section of this manuscript. Archived data are provided in Scharf et al. (2024).

References

Agard, P., Omrani, J., Jolivet, L., Whitechurch, H., Vrielynck, B., Spakman, W., Monié, P., Meyer, B., Wortle, R., 2011. Zagros orogeny: a subduction-dominated process. Geol. Mag. 148 (5–6), 692–725.

Aldega, L., Carminati, E., Scharf, A., Mattern, F., Al-Wardi, M., 2017. Estimating original thickness and extent of the Semail Ophiolite in the eastern Oman Mountains by paleothermal indicators. Mar. Pet. Geol. 84, 18–33.

Allen, P.A., 2007. The huqf supergroup of Oman: Basin development and context for neoproterozoic glaciation. Earth Sci. Rev. 84, 139–185.

Allmendinger, R.W., Cardozo, N., Fisher, D., 2012. Structural Geology Algorithms: Vectors and Tensors in Structural Geology. Cambridge University Press.

Banks, D.A., Yardley, B.W.D., Campbell, A.R., Jarvis, K.E., 1994. REE composition of an aqueous magmatic fluid: a fluid inclusion study from the Capitan Pluton, New Mexico, USA. Chem. Geol. 113 (3–4), 259–272.

Banner, J.L., Hanson, G.N., Meyers, W.J., 1988. Rare earth element and Nd isotopic variations in regionally extensive dolomites from the Burlington-Keokuk Formation (Mississippian); implications for REE mobility during carbonate diagenesis. J. Sediment. Res. 58 (3), 415–432.

Bau, M., 1991. Rare-earth element mobility during hydrothermal and metamorphic fluid-rock interaction and the significance of the oxidation state of europium. Chem. Geol. 93 (3–4), 219–230.

Bau, M., Dulski, P., 1995. Comparative study of yttrium and rare-earth element behaviours in fluorine-rich hydrothermal fluids. Contrib. Mineral. Petrol. 119, 213–223.

Bau, M., Möller, P., 1992. Rare earth element fractionation in metamorphogenic hydrothermal calcite, magnesite and siderite. Mineral. Petrol. 45, 231–246.

Bau, M., Koschinsky, A., Dulski, P., Hein, J.R., 1996. Comparison of the partitioning behaviours of yttrium, rare earth elements, and titanium between hydrogenetic marine ferromanganese crusts and seawater. Geochim. Cosmochim. Acta 60 (10), 1709–1725.

Bau, M., Möller, P., Dulski, P., 1997. Yttrium and lanthanides in eastern Mediterranean seawater and their fractionation during redox-cycling. Mar. Chem. 56 (1–2), 123–131.

Bau, M., Balan, S., Schmidt, K., Koschinsky, A., 2010. Rare earth elements in mussel shells of the Mytilidae family as tracers for hidden and fossil high-temperature hydrothermal systems. Earth Planet. Sci. Lett. 299 (3–4), 310–316.

Beaudoin, N.E., Lacombe, O., Hoareau, G., Callot, J-P., 2022. How the geochemistry of syn-kinematic calcite cement depicts past fluid flow and assists structural interpretations: a eview of concepts and applications in orogenic forelands. Geol. Mag. 159, 2157–2190.

Beurrier, M., Béchennec, F., Rabu, D., Hutin, G., 1986. Geological Map of Rustaq, Sheet NF 40-03D, Scale 1:100,000, with Explanatory Notes: Directorate General of Minerals. Oman Ministry of Petroleum and Minerals.

Blendinger, W., van Vliet, A.T., Hughes Clarke, M.W., 1990. Updoming, rifting and continental margin development during the Late Paleozoic in northern Oman. In: Robertson, A.H.F., Searle, M.P., Ries, A.C. (Eds.), The Geology and Tectonics of the Oman Region. Geological Society of London, Special Publication, 49, pp. 27–37.
Bodnar, R.J., 1993. Revised equation and table for determining the freezing point depression of H_2O-NaCl solutions. Geochim. Cosmochim. Acta 57, 683–684.
Bolhar, R., Van Kranendonk, M.J., 2007. A non-marine depositional setting for the northern Fortescue Group, Pilbara Craton, inferred from trace element geochemistry of stromatolitic carbonates. Precambrian Res. 155 (3–4), 229–250.
Bolhar, R., Kamber, B.S., Moorbath, S., Fedo, C.M., Whitehouse, M.J., 2004. Characterisation of early archaean chemical sediments by trace element signatures. Earth Planet. Sci. Lett. 222 (1), 43–60.
Bolhar, R., Hofmann, A., Siahi, M., Feng, Y.X., Delvigne, C., 2015. A trace element and Pb isotopic investigation into the provenance and deposition of stromatolitic carbonates, ironstones and associated shales of the~ 3.0 Ga Pongola Supergroup, Kaapvaal Craton. Geochim. Cosmochim. Acta 158, 57–78.
Bons, P.D., Cao, D., de Riese, T., Gonzalez-Esvertit, E., Koehn, D., Naaman, I., Sachau, T., Tian, H., Gomez-Rivas, E., 2023. A review of natural hydrofractures in rocks. Geol. Mag. 149, 1952–1977.
Breton, J.-P., Béchennec, F., Le Métour, J., Moen-Maurel, L., Razin, P., 2004. Eoalpine (cretaceous) evolution of the Oman Tethyan continental margin: insights from a structural field study in Jabal Akhdar (Oman Mountains). GeoArabia 9 (2), 41–58.
Burkhard, M., 1993. Calcite twins, their geometry, appearance and significance as stress-strain markers and indicators of tectonic regime: a review. J. Struct. Geol. 15, 351–358.
Callegari, I., Scharf, A., Mattern, F., Bauer, W., Pinto, A.J., Scharf, K., Rarivoarison, H., Al-Kindi, M.H., 2020. Gondwana accretion tectonics and implications for the geodynamic evolution of eastern Arabia: first structural evidence of the existence of the Cadomian Orogeny in Oman (Jabal Akhdar Dome, Central Oman Mountains). J. Asian Earth Sci. 187, 104070. https://doi.org/10.1016/j.jseaes.2019.104070.
Callegari, I., Scharf, A., Mattern, F., Scharf, K., 2022. Tectonic transition from thrusting to polyphase non-confining deformation within the Semail Ophiolite along the sinistral, transtensional Issmaiya Fault Zone (Sultanate of Oman). Journal of Asian Earth Sciences 224 (5), 105007. https://doi.org/10.1016/j.jseaes.2021.105007.
Cardozo, N., Allmendinger, R.W., 2013. Spherical projections with OSXStereonet. Comnput. Geosci. 51, 193–205.
Carminati, E., Aldega, L., Smeraglia, L., Scharf, A., Mattern, F., Albert, R., Gerdes, A., 2020. Tectonic evolution of the Northern Oman Mountains, part of the Strait of Hormuz Syntaxis: new structural and paleothermal analyses and U-Pb dating of synkinematic calcite. Tectonics 39 (4), e2019TC005936.
Chacko, T., Mayeda, T.K., Clayton, R.N., Goldsmith, J.R., 1991. Oxygen and carbon isotope fractionations between CO2 and calcite. Geochim. Cosmochim. Acta 50, 2867–2882.
Chacko, T., Cole, D.R., Horita, J., 2001. Equilibrium oxygen, hydrogen and carbon isotope fractionation factors applicable to geological systems. Rev. Mineral. Geochem. 43 (1), 1–81.
Chauvet, F., Dumont, T., Basile, C., 2009. Structures and timing of Permian rifting in the Central Oman Mountains (Saih Hatat). Tectonophysics 475, 563–574.
Corradetti, A., Spina, V., Tavani, S., Ringenbach, J.C., Sabbatino, M., Razin, P., Laurant, O., Brichau, S., Mazzoli, S., 2020. Late-stage tectonic evolution of the Al-Hajar Mountains, Oman: new constraints from Palaeogene sedimentary units and low-temperature thermochronometry. Geol. Mag. 1-14. https://doi.org/10.1017/S0016756819001250.
Craddock, P.R., Bach, W., Seewald, J.S., Rouxel, O.J., Reeves, E., Tivey, M.K., 2010. Rare earth element abundances in hydrothermal fluids from the Manus Basin, Papua New Guinea: indicators of sub-seafloor hydrothermal processes in back-arc basins. Geochim. Cosmochim. Acta 74 (19), 5494–5513.
De Baar, H.J., Bacon, M.P., Brewer, P.G., Bruland, K.W., 1985. Rare earth elements in the Pacific and Atlantic Oceans. Geochim. Cosmochim. Acta 49 (9), 1943–1959.
Debruyne, D., Hulsbosch, N., Muchez, P., 2016. Unraveling rare earth element signatures in hydrothermal carbonate minerals using a source–sink system. Ore Geol. Rev. 72, 232–252.
Derry, L.A., Kaufman, A.J., Jacobsen, S.B., 1992. Sedimentary cycling and environmental change in the late Proterozoic: evidence from stable and radiogenic isotopes. Geochim. Cosmochim. Acta 56 (3), 1317–1329.
Drost, K., Chew, D., Petrus, J.A., Scholze, F., Woodhead, J.D., Schneider, J.W., Harper, D. A., 2018. An image mapping approach to U-Pb LA-ICP-MS carbonate dating and applications to direct dating of carbonate sedimentation. Geochem. Geophys. Geosyst. 19 (12), 4631–4648.
Droste, H., 2014. Petroleum geology of the sultanate of Oman. In: Marlow, L., Kendall, C., Yose, L. (Eds.), Petroleum Systems of the Tethyan Region, American Association of Petroleum Geologists Memoir, vol. 106, pp. 713–755. https://doi.org/10.1036/12431870M1063039.
Evans, M.J., Derry, L.A., France-Lanord, C., 2008. Degassing of metamorphic carbon dioxide from the Nepal Himalaya. Geochem. Geophys. Geosyst. 9, Q04021. https://doi.org/10.1029/2007GC001796.
Ferrill, D.A., Morris, A.P., Evans, M.A., Burkhar, M., Groshong Jr., R.H., Onasch, C.M., 2004. Calcite twin morphology: a low-temperature deformation geothermometer. J. Struct. Geol. 26, 1521–1529.
Forbes, G.A., Jansen, H.S.M., Schreurs, J., 2010. Lexicon of Oman subsurface stratigraphy. Reference guide to the stratigraphy of Oman's Hydrocarbon basins. GeoArabia 373. Special Publication 5 by Gulf Petro Link.
Fournier, M., Lepvrier, C., Razin, P., Jolivet, L., 2006. Late cretaceous to paleogene post-obduction extension and subsequent neogene compression in the Oman Mountains. GeoArabia 11 (4), 17–40.
Gao, S., Liu, X., Yuan, H., Hattendorf, B., Günther, D., Chen, L., Hu, S., 2002. Determination of forty two major and trace elements in USGS and NIST SRM glasses by laser ablation inductively coupled plasma mass spectrometry. Geostand. Newslett. 26 (2), 181–196.
Glennie, K.W., Boeuf, M.G.A., Hughes Clarke, M.W., Moody-Stuart, M., Pilaar, W., Reinhardt, B.M., 1974. Geology of the Oman Mountains. Koninklijk Nederlands Geologisch en Mijnbouwkundig Genootschap. Transactions 31 (1), 423.
Grobe, A., Virgo, S., von Hagke, C., Urai, J.L., Littke, R., 2018. Multiphase structural evolution of a continental margin during obduction orogeny. Tectonics 37, 88–913.
Haas, J.R., Shock, E.L., Sassani, D.C., 1995. Rare earth elements in hydrothermal systems: estimates of standard partial molal thermodynamic properties of aqueous complexes of the rare earth elements at high pressures and temperatures. Geochim. Cosmochim. Acta 59 (21), 4329–4350.
Hansman, R.J., Ring, U., Thomson, S.N., den Brock, B., Stübner, K., 2017. Late Eocene uplift of the Al Hajar Mountains, Oman, supported by stratigraphic and low-temperature thermochronology. Tectonics 36 (12), 3081–3109. https://doi.org/10.1002/2017TC004672.
Hansman, R.J., Albert, R., Gerdes, A., Ring, U., 2018. Absolute ages of multiple generations of brittle structures by U-Pb datin of calcite. Geology 46 (3), 207–210.
Hecht, L., Freiberger, R., Gilg, H.A., Grundmann, G., Kostitsyn, Y.A., 1999. Rare earth element and isotope (C, O, Sr) characteristics of hydrothermal carbonates: genetic implications for dolomite-hosted talc mineralization at Göpfersgrün (Fichtelgebirge, Germany). Chem. Geol. 155 (1–2), 115–130.
Hill, C.A., Polyak, V.J., Asmerom, Y., Provencio, P., 2016. Constraints on a late cretaceous uplift, denudation, and incision of the Grand Canyon region, southwestern Colorado Plateau, USA, from U-Pb dating of lacustrine limestone. Tectonics 35 (4), 896–906.
Hoefs, J., 2021. Isotope fractionation processes of selected elements. Stable Isotope Geochem. 49–265.
Jochum, K.P., Weis, U., Stoll, B., Kuzmin, D., Yang, Q., Raczek, I., Günther, D., 2011. Determination of reference values for NIST SRM 610-617 glasses flowing ISO guidelines. Geostand. Geoanal. Res. 34 (4), 397–429.
Kamber, B.S., Webb, G.E., 2001. The geochemistry of late Archaean microbal carbonate: implications for ocean chemistry and continental erosion history. Geochim. Cosmochim. Acta 65 (1), 2509–2525.
Kamber, B.S., Greig, A., Collerson, K.D., 2005. A new estimate for the composition of weathered young upper continental crust from alluvial sediments, Queensland, Australia. Geochim. Cosmochim. Acta 69 (4), 1041–1058.
Karabacak, V., Sançar, T., Yildirim, G., Uysal, I.T., 2022. When did the North Anatolian fault reach southern Marmara, Turkey? Geology 50 (4), 432–436. https://doi.org/10.1130/G49726.1.
Kennedt, L.A., White, J.C., 2001. Low-temperature recrystallization in calcite: mechanism and consequences. Geology 29, 1027–1030.
Kramers, J.D., Tolstikhin, I.N., 1997. Two terrestrial lead isotope paradoxes, forward transport modelling, core formation and the history of the continental crust. Chem. Geol. 139 (1–4), 75–110.
Le Métour, J., Michel, J.C., Béchennec, F., Platel, J.P., Roger, J., 1995. Geologogy and Mineral Wealth of the Sultanate of Oman. Sultanate of Oman Ministry of Petroleum and Minerals, Directorate of Minerals, M.P.M. Geological Documents, p. 286.
Lee, J.H., Byrne, R.H., 1992. Examination of comparative rare earth element complexation behavior using linear free-energy relationships. Geochim. Cosmochim. Acta 56 (3), 1127–1137.
Mann, A., Hanna, S.S., 1990. The tectonic evolution of pre-permian rocks, Central and Southeastern Oman Mountains. In: Robertson, A.H.F., Searle, M.P., Ries, A.C. (Eds.), The Geology and Tectonics of the Oman Region. Geological Society of London, Special Publication, 49, pp. 307–325.
Mattern, F., Scharf, A., 2019. Transition from the Hajir Formation to the Muaydin Formation: a facies change coinciding with extensional, syndepositional faulting (Ediacaran, Jabal Akhdar Dome, Central Oman Mountains). J. Afr. Earth Sci. 152, 237–244.
Mattern, F., Scharf, A., Pracejus, B., Al-Rhabi, S., 2024. Pangea rifting in eastern Arabia – New insights from mafic dikes of the Saih Hatat Dome (Oman Mountains). Arab. J. Geosci. 17 (12), 334.
Migdisov, A.A., Williams-Jones, A.E., 2014. Hydrothermal transport and deposition of the rare earth elements by fluorine-bearing aqueous liquids. Mineral. Deposita 49, 987–997.
Moffett, J.W., 1990. Microbially mediated cerium oxidation in sea water. Nature 345 (6274), 421–423.
Morgan, J.W., Wandless, G.A., 1980. Rare earth element distribution in some hydrothermal minerals: evidence for crystallographic control. Geochim. Cosmochim. Acta 44 (7), 973–980.
Mozley, P.S., Wersin, P., 1992. Isotopic composition of siderite as an indicator of depositional environment. Geology 20 (9), 817–820.
Nuriel, P., Rosenbaum, G., Zhao, J.X., Feng, Y., Golding, S.D., Villemant, B., Weinberger, R., 2012. U-Th dating of striated fault planes. Geology 40, 647–650.
Nuriel, P., Weinberger, R., Kylander-Clark, A.R.C., Hacker, B.R., Craddock, J.P., 2017. The onset of the Dead Sea transform based on calcite age-strain analyses. Geology 45 (7), 587–590.
O'Neil, J.R., Clayton, R.N., Mayeda, T.K., 1969. Oxygen isotope fractionation in divalent metal carbonates. J. Chem. Phys. 51, 5547–5558.
Ostrander, C.M., Bjerrum, C.J., Ahm, A.S., Stenger, S.R., Bergmann, K.D., El-Ghali, M.A., Harthi, A.R., Aisri, Z., Nielsen, S.G., 2023. Widespread seafloor anoxia during generation of the Ediacaran Shuram carbon isotope excursion. Geobiology 21 (5), 556–570.

Paton, C., Woodhead, J.D., Hellstrom, J.C., Hergt, J.M., Greig, A., Maas, R., 2010. Improved laser ablation U-Pb zircon geochronology through robust downhole fractionation corrections. Geochem. Geophys. Geosyst. 11 (3).
Paton, C., Hellstrom, J., Paul, B., Woodhead, J., Hergt, J., 2011. Iolite: Freeware for the visualization and processing of mass spectrometric data. J. Anal. At. Spectrom. 26 (12), 2508–2518.
Pourtier, E., Devidal, J.L., Gibert, F., 2010. Solubility measurements of synthetic neodymium monazite as a function of temperature at 2 kbars, and aqueous neodymium speciation in equilibrium with monazite. Geochim. Cosmochim. Acta 74 (6), 1872–1891.
Rabu, D., Béchennec, F., Beurrier, M., Hutin, G., 1986. Geological Map of Nakhl, Sheet NF40-3E, Scale: 1:100,000, with Explanatory Notes: Directorate General of Minerals. Oman Ministry of Petroleum and Minerals.
Rasbury, E.T., Cole, J.M., 2009. Directly dating geologic events: U-Pb dating of carbonates. Rev. Geophys. 47 (3).
Ring, U., Bolhar, R., 2020. Tilting, uplift, volcanism and disintegration of the south German block. Tectonophysics 795, 228611.
Ring, U., Fassoulas, C., Uysal, I.T., Bolhar, R., Tong, K., Todd, A., 2022. Nappe imbrication within the phyllite-quartzite unit of west crete: implications for sustained high-pressure metamorphism in the hellenide subduction Orogen, Greece. Tectonics 41 (11), e2022TC007430.
Ring, U., Glodny, J., Hansman, R., Scharf, A., Mattern, F., Callegari, I., van Hinsbergen, D., Wilner, A., Hong, Y., 2024. The Samail subduction zone dilemma: geochronology of high-pressure rocks from the Saih Hatat windiw, Oman, reveals juxtaposition of two subduction zones with contrasting thermal histories. Earth-Sci. Rev. 250, 104711.
Roberts, N.M.W., Holdsworth, R.E., 2022. Timescales of faulting through calcite geochronology: a review. J. Struct. Geol. 158, 104578.
Roberts, N.M.W., Rasbury, E.T., Parrish, R.R., Smith, C.J., Horstwood, M.S., Condon, D. J., 2017. A calcite reference material for LA-ICP-MS U-Pb geochronology. Geochem. Geophys. Geosyst. 18 (7), 2807–2814.
Roberts, N.M.W., Drost, K., Horstwood, M.S., Condon, D.J., Chew, D., Drake, H., Milodowski, A.E., McLean, N.M., Smye, A.J., Walker, R.J., Haslam, R., 2020. Laser ablation inductively coupled plasma mass spectrometry (LA-ICP-MS) U–Pb carbonate geochronology: strategies, progress, and limitations. Geochronology 2 (1), 33–61.
Roedder, E., 1984. Volume 12: Fluid Inclusions, Reviews in Mineralogy 12, 644. Mineralogical Society of America, Washington, D.C.
Saddiqi, O., Michard, A., Goffé, B., Poupeau, G., Oberhänsli, R., 2006. Fission-track thermochronology of the Oman Mountains continental widows, and current problems of tectonic interpretation. Bull. Soc. Géol. France 177 (3), 127–134. https://doi.org/10.2113/gssgfbull.177.3.127.
Scharf, A., Callegari, I., Mattern, F., Scharf, K., Carminati, E., 2021a. Triple folded surface morphology of neoproterozoic rocks (Jabal Akhdar Dome, Oman Mountains) – Insights into buttressing effects and regional tectonics. J. Asian Earth Sci. 221, 104942. https://doi.org/10.1016/j.jseaes.2021.104942.
Scharf, A., Mattern, F., Al-Wardi, M., Frijia, G., Moraetis, D., Pracejus, B., Bauer, W., Callegari, I., 2021b. The geology and tectonics of the Jabal Akhdar and Saih Hatat domes, Oman Mountains. Geol. Soc. Lond. Mem. M54 (1), 124. https://doi.org/10.1144/M54.
Scharf, A., Bailey, C.M., Bolhar, R., Mattern, F., Ring, U., 2022a. Post-obduction listwaenite genesis in the Oman Mountains inferred from structural analysis and U-Pb carbonate dating. Earth Planet. Sci. Lett. 595, 117756. https://doi.org/10.1016/j.epsl.2022.117756.
Scharf, A., Mattern, F., Bolhar, R., Callegari, I., Mattern, P., Ring, U., 2022b. Oligocene/early miocene E/W-shortening in the Oman Mountains related to oblique Arabia-India convergence. Tectonics 41 (12), e2022TC007271. https://doi.org/10.1029/2022TC007271.
Scharf, A., Bolhar, R., Uysal, T.I., Mattern, F., Callegari, I., Bozkaya, G., Baublys, K., 2024. A vein-hosted carbonate geochemical, isotopic and geochronological record of late miocene to pleistocene hydrothermal activity in the Hajar Mountains (Jabal Akhdar Dome, Sultanate of Oman) [Dataset]. Mendeley Data 1. https://doi.org/10.17632/b9kkc3dpkp.1.
Shannon, R.D., 1976. Revised effective ionic radii and systematic studies of interatomic distances in halides and chalcogenides. Acta Crystallogr. Sect. A: Cryst. Phys., Diffr., Theor. Gen. Crystallogr. 32 (5), 751–767.
Sibson, R.H., 1986. Brecciation processes in fault zones: inferences from earthquake rupturing. Pure Appl. Geophys. 124, 159–175.
Smeraglia, L., Aldega, L., Bernasconi, S.M., Billi, A., Boschi, C., Caracausi, A., Carminate, E., Franchini, S., Rizzo, A.L., Rossetti, F., Vignaroli, G., 2020. The role of trapped fluids during the development and deformation of a carbonate/shale intra-wedge tectonic mélange (Mt. Massico, Southern Apennines, Italy). J. Struct. Geol. 138, 104086.
Sverjensky, D.A., 1984. Europium redox equilibria in aqueous solution. Earth Planet. Sci. Lett. 67 (1), 70–78.
Tanaka, K., Kawabe, I., 2006. REE abundances in ancient seawater inferred from marine limestone and experimental REE partition coefficients between calcite and aqueous solution. Geochem. J. 40 (5), 425–435.
Tsay, A., Zajacz, Z., Sanchez-Valle, C., 2014. Efficient mobilization and fractionation of rare-earth elements by aqueous fluids upon slab dehydration. Earth Planet. Sci. Lett. 398, 101–112.
Uysal, I.T., Fengm, Y.X., Zhao, J.X., Isik, V., Nuriel, P., Golding, S.D., 2009. Hydrothermal CO2 degassing in seismically active zones during the late quaternary. Chem. Geol. 265 (3–4), 442–454.
Van Sijl, J., Allan, N.L., Davies, G.R., Van Westrenen, W., 2009. Molecular modelling of rare earth element complexation in subduction zone fluids. Geochim. Cosmochim. Acta 73 (13), 3934–3947.
Veksler, I.V., 2004. Liquid immiscibility and its role at the magmatic–hydrothermal transition: a summary of experimental studies. Chem. Geol. 210 (1–4), 7–31.
Vermeesch, P., 2018. IsoplotR: a free and open toolbox for geochronology. Geosci. Front. 9 (5), 1479–1493.
Weidle, C., Wiesenberg, L., Scharf, A., Agard, P., El-Sharkaway, A., Krüger, F., Meier, T., 2023. Lithospheric evolution of eastern Arabia based on surface wave and receiver function analyses. Earth Planet. Sci. Lett. 611, 118145. https://doi.org/10.1016/j.epsl.2023.118145.
Wood, S.A., 2004. The hydrothermal geochemistry of the rare Earth elements. Gangue 8, 1–7.
Woodhead, J., Petrus, J., 2019. Exploring the advantages and limitations of in situ U–Pb carbonate geochronology using speleothems. Geochronology 1 (1), 69–84.
Yardley, B.W., Bodnar, R.J., 2014. Fluids in the continental crust. Geochem. Perspect. 3 (1), 1–2.
Zuccari, C., Vignaroli, G., Callegari, I., Nestola, F., Novella, D., Giuntoil, F., Guillong, M., Viola, G., 2023. Forming and preserving aragonite in shear zones: first report of blueshist facies metamorphism in the Jabal Akhdar Dome, Oman Mountains. Geology 51 (5), 454–459.